

A Measurement of the  
Neutron Electric Form Factor.

Robin J Watson

Presented as a Thesis for the Degree of Doctor of Philosophy

Department of Physics and Astronomy,

University of Glasgow,

June 1997.

ProQuest Number: 13832062

All rights reserved

INFORMATION TO ALL USERS

The quality of this reproduction is dependent upon the quality of the copy submitted.

In the unlikely event that the author did not send a complete manuscript and there are missing pages, these will be noted. Also, if material had to be removed, a note will indicate the deletion.



ProQuest 13832062

Published by ProQuest LLC (2019). Copyright of the Dissertation is held by the Author.

All rights reserved.

This work is protected against unauthorized copying under Title 17, United States Code  
Microform Edition © ProQuest LLC.

ProQuest LLC.  
789 East Eisenhower Parkway  
P.O. Box 1346  
Ann Arbor, MI 48106 – 1346

Thesis 10986  
Copy 1



## Abstract

The electromagnetic form factors of the neutron and proton,  $G_E^{n,p}$  and  $G_M^{n,p}$ , are of fundamental importance to our understanding of their internal structure, and provide useful constraints for models of nucleon structure. Until recently, measurements of the neutron electric form factor,  $G_E^n$ , were hampered by the model dependence of e-D scattering data, and from the small size of  $G_E^n$  relative to  $G_M^n$ . New techniques using polarised electron beams offer improved methods of measurement where  $G_E^n$  appears in the product  $G_E^n G_M^n$  as an interference term.

This thesis comprises such a measurement, which was performed recently at the University of Mainz's MAMI-B electron accelerator facility, using the reaction  $\vec{e}(D, e'\vec{n})p$ , where the recoil neutron transverse polarisation component  $P_x$  gives a measure of  $G_E^n$ .

The thesis includes a study of the neutron polarimeter using a Monte-Carlo model which provides an estimate of the analysing power. The model was developed using the particle physics simulation package GEANT and the neutron detection efficiency program STANTON, requiring substantial modification to allow the study of the passage of neutrons through a complex detector geometry, and to simulate the asymmetric neutron distribution following p(n,np) scattering. The simulation results are in good agreement with those of an independent simulation ([21]). The polarimeter is calibrated by the use of a spin-precession technique, in which the longitudinal  $P_z$  component of neutron polarisation is precessed by a magnetic field of integral  $\sim 1.5Tm$  by ninety degrees, and hence becomes transverse and measurable by the polarimeter. The  $P_z$  component is essentially

independent of  $G_E^n$  and is calculable, allowing the polarimeter analysing power to be determined. Analysing powers of around 15% are found, in good agreement with the results of the Monte-Carlo simulation. A preliminary measurement of  $G_E^n$  is made at  $Q^2 = 9.4 fm^{-2}$  by measuring the transverse  $P_x$  component.

## Declaration

The data presented in this thesis were obtained in collaboration with colleagues from the Institut für Kernphysik, Universität Mainz, the Physikalisches Institut, Universität Tübingen and the Department of Physics and Astronomy, University of Glasgow. I participated fully in the preparation and execution of the experiment. The computer simulation, and the analysis and interpretation of the experimental data, are entirely my own work. This thesis was composed by myself.

**Robin J Watson**

## Acknowledgements

Firstly, I would like to express my thanks to my supervisor Dr. Jim Kellie, and to Dr. John Annand for their help and advice over the past four years or so.

I am grateful to the members of the Institut für Kernphysik, Mainz, for giving me the opportunity to participate in the A3 experiment, and especially to students past and present Dr. Andreas Frey, Dr. Dietmar Eyl, Michael Ostrick, Carsten Herberg and Rüdiger Sprengard, and to Drs. Fritz Klein and Hartmut Schmieden. Thanks also to the collaborators from Tübingen and the Institut für Physik, Mainz.

I would like to thank the remaining Glasgow A3 collaborators Dr. Ken Livingston and Prof. Bob Owens, and all the students and staff of the Glasgow Nuclear Physics Group.

I am indebted to the Engineering and Physical Sciences Research Council and to the Nuclear Physics Group for providing financial support and travel expenses during my time as a student.

# Contents

|          |  |           |
|----------|--|-----------|
| <b>1</b> | <b>Introduction</b>                            | <b>1</b>  |
| <b>2</b> | <b>Theory and Review</b>                       | <b>4</b>  |
| 2.1      | The Neutron . . . . .                          | 4         |
| 2.2      | Form Factors . . . . .                         | 5         |
| 2.3      | Measurements of neutron form factors . . . . . | 8         |
| 2.3.1    | Thermal neutron scattering . . . . .           | 8         |
| 2.3.2    | Elastic e-D scattering . . . . .               | 8         |
| 2.3.3    | Quasi-elastic e-D scattering . . . . .         | 9         |
| 2.4      | Polarised electron beam methods . . . . .      | 10        |
| 2.5      | Nuclear Binding Effects . . . . .              | 11        |
| 2.6      | Comparison of experiment and theory . . . . .  | 13        |
| <b>3</b> | <b>Experimental Apparatus</b>                  | <b>16</b> |
| 3.1      | The Polarised Electron Source . . . . .        | 18        |
| 3.2      | The Electron Accelerator . . . . .             | 19        |
| 3.3      | The Spin-rotator. . . . .                      | 21        |
| 3.4      | Electron Polarimeters . . . . .                | 22        |
| 3.5      | The Liquid Deuterium Target. . . . .           | 24        |
| 3.6      | The Electron Detector. . . . .                 | 24        |
| 3.7      | Data Acquisition System . . . . .              | 25        |

|          |  |           |
|----------|--|-----------|
| <b>4</b> | <b>The Neutron Polarimeter</b>                   | <b>28</b> |
| 4.1      | Introduction . . . . .                           | 28        |
| 4.2      | The Spin-Precession Method . . . . .             | 33        |
| 4.3      | A Monte-Carlo Simulation . . . . .               | 35        |
| 4.4      | A Kinematical Trigger . . . . .                  | 43        |
| <b>5</b> | <b>Data Analysis</b>                             | <b>48</b> |
| 5.1      | Neutron Detector Calibrations . . . . .          | 48        |
| 5.1.1    | Timing Corrections . . . . .                     | 48        |
| 5.1.2    | Position and time calibrations . . . . .         | 55        |
| 5.2      | The electron detector . . . . .                  | 60        |
| 5.2.1    | The lead-glass pulse height . . . . .            | 60        |
| 5.3      | Selection of quasi-elastic events . . . . .      | 62        |
| 5.4      | Neutron Scattering Reconstruction . . . . .      | 64        |
| 5.5      | Asymmetry Calculation . . . . .                  | 66        |
| 5.6      | Enrichment of n-p scattering events . . . . .    | 68        |
| 5.7      | Pulse-height Calibration . . . . .               | 69        |
| 5.7.1    | Cosmic Rays . . . . .                            | 69        |
| 5.7.2    | Drop corrections . . . . .                       | 70        |
| 5.7.3    | Relativistic particles . . . . .                 | 72        |
| 5.7.4    | The Enrichment Procedure . . . . .               | 72        |
| <b>6</b> | <b>Results and Conclusion</b>                    | <b>75</b> |
| 6.1      | Polarimeter Analysing Power Measurement. . . . . | 75        |
| 6.2      | Zero-Field Asymmetries and $G_E^n$ . . . . .     | 79        |
| 6.3      | Nuclear Binding Effects . . . . .                | 80        |
| 6.4      | Sources of systematic error . . . . .            | 82        |
| 6.5      | Conclusion . . . . .                             | 86        |

# List of Figures

|     |  |    |
|-----|--|----|
| 2.1 | Existing $G_E^n$ data . . . . .  | 9  |
| 2.2 | Electron-neutron scattering . . . . .                                  | 11 |
| 2.3 | Recent $G_E^n$ measurements . . . . .                                  | 14 |
| 3.1 | The experimental set-up . . . . .                                      | 17 |
| 3.2 | Band structure of GaAs . . . . .                                       | 19 |
| 3.3 | The Race-Track Microtron . . . . .                                     | 20 |
| 3.4 | The Spin Rotator . . . . .   | 22 |
| 3.5 | The Møller Polarimeter . . . . .                                       | 23 |
| 3.6 | Trigger electronics . . . . .  | 26 |
| 4.1 | A plan view of the neutron polarimeter . . . . .                       | 29 |
| 4.2 | A scintillator block . . . . .   | 30 |
| 4.3 | Coordinate frame for neutron scattering . . . . .                      | 31 |
| 4.4 | Analysing power for n-p scattering . . . . .                           | 32 |
| 4.5 | The neutron spin-precession method . . . . .                           | 34 |
| 4.6 | Initial neutron momentum distribution . . . . .                        | 37 |
| 4.7 | The ratios $Q_1$ and $Q_2$ . . . . .                                   | 39 |
| 4.8 | Distribution of events in the neutron and electron detectors . . . . . | 44 |
| 4.9 | Neutron kinetic energy against electron pulse height . . . . .         | 45 |

|   |    |
|---|----|
| 4.10 Neutron kinetic energy against electron pulse height at forward angles . . . . .             | 46 |
| 5.1 A neutron TDC spectrum . . . . .  | 49 |
| 5.2 The leading-edge walk effect. . . . .   | 51 |
| 5.3 The walk effect in a lead-glass TDC. . . . .  | 52 |
| 5.4 The walk effect in a neutron TDC. . . . .   | 54 |
| 5.5 $a^{-\frac{1}{2}}$ versus time . . . . .  | 55 |
| 5.6 A scintillator block . . . . .  | 56 |
| 5.7 Neutron TDC spectra before and after time corrections. . . . .                                | 57 |
| 5.8 A neutron TDC spectrum . . . . .  | 59 |
| 5.9 Scattering geometry . . . . .   | 59 |
| 5.10 Electron pulse height . . . . .  | 62 |
| 5.11 Ratio of measured and theoretical neutron energies . . . . .                                 | 63 |
| 5.12 Ratio of measured and theoretical neutron energies from the Monte-Carlo simulation . . . . . | 63 |
| 5.13 N2 time versus N1 time . . . . .   | 64 |
| 5.14 Double scattering geometry . . . . .   | 65 |
| 5.15 Neutron scattered angle $\phi_n'$ . . . . .  | 66 |
| 5.16 Polarisation vectors after $45^\circ$ spin precession. . . . .                               | 67 |
| 5.17 Asymmetry as a function of azimuthal angle. . . . .  | 69 |
| 5.18 Parametrisation of droop in an N1 block. . . . .   | 71 |
| 5.19 Relativistic peak in a neutron detector TDC spectrum. . . . .                                | 73 |
| 5.20 The ratios $Q_1$ and $Q_2$ . . . . .   | 74 |
| 5.21 The ratios $Q_1$ and $Q_2$ from the MC simulation. . . . .                                   | 74 |
| 6.1 Asymmetry as a function of azimuthal angle. . . . .   | 76 |
| 6.2 Asymmetry as a function of azimuthal angle. . . . .   | 77 |

|     |  |    |
|-----|--|----|
| 6.3 | The angles $\theta_{nq}$ and $\phi_r$ . . . . .                      | 81 |
| 6.4 | The $\phi_r$ (left) and $\theta_{nq}$ (right) distributions. . . . . | 81 |
| 6.5 | The result of the present experiment . . . . .                       | 85 |

# List of Tables

|     |   |    |
|-----|---|----|
| 4.1 | Monte-Carlo results for 0.5ns resolution . . . . .            | 40 |
| 4.2 | Monte-Carlo results for 1.0ns resolution . . . . .            | 40 |
| 4.3 | Monte-Carlo results for 2.0ns resolution . . . . .            | 42 |
| 6.1 | Analysing power under various software cuts . . . . .         | 78 |
| 6.2 | $G_E^n$ under various software cuts . . . . .                 | 79 |
| 6.3 | The effect of electron pulse height cuts on $G_E^n$ . . . . . | 80 |
| 6.4 | $\theta_{nq}$ dependence of $G_E^n$ . . . . .                 | 82 |
| 6.5 | $\phi_r$ dependence of $G_E^n$ . . . . .                      | 83 |
| 6.6 | $\phi_r$ and $\theta_{nq}$ dependence of $G_E^n$ . . . . .    | 83 |

# Chapter 1

## Introduction

The atomic nature of matter was first proposed by Democritus (c.450 BC) who suggested that all substances were composed of combinations of indivisible atoms of different kinds. The idea was revived in the 19th Century by Dalton when compounds were found to be divisible into definite ratios of the constituent elements. The discovery of the electron by J.J.Thomson, together with other forms of radiation, pointed to the atom having some form of substructure, and the proton's discovery shortly afterwards suggested the atom to be composed of equal numbers of protons and electrons.

Rutherford's scattering experiments led to the development of the nuclear model of the atom, where the positive protons, possessing most of the atom's mass, were contained in a small dense nucleus, surrounded by a cloud of negatively charged electrons. To account for the observed masses and charges of elements, it was supposed that a nucleus of mass  $A$  and charge  $Z$  consisted of  $A$  protons, partially neutralised by  $(A-Z)$  nuclear electrons, with a further  $Z$  atomic electrons orbiting the core.

The observed spin of the  $^{14}\text{N}$  nucleus remained a problem for this model, according to which the 21 nuclear constituents would lead to a half-integer overall

nuclear spin, at odds with the observed value of 1. The discovery of the neutron in the 1930s solved this problem and provided a simpler explanation of observed nuclear properties.

Measurements of their magnetic moments showed that nucleons possessed an anomalous component, differing from that predicted by Dirac theory for point particles, and suggesting that they had some sort of internal structure. The scattering of thermal neutrons from atomic electrons in the 1940s established the charge radius of the neutron, and indicated the existence of a positive core surrounded by a region of negative charge. One way of viewing this was to consider the neutron as spending part of its time as a proton and a negative pion, accounting for the observed charge distribution and the overall neutrality.

The proliferation of new particles in the 1950s led to the development of the quark model, in which all observed hadrons consisted of combinations of 3 (and later 6) different quark ‘flavours’. According to this model the neutron would consist of a *udd* combination, giving an overall charge of zero. Deep inelastic scattering experiments in the 1960s of electrons on protons provided evidence for point-like particles inside the nucleon.

The behaviour of quarks and gluons can be described by Quantum Chromodynamics (QCD). At very small scales, perturbative methods can be used to obtain solutions. At the scales applicable to nucleons, however, such methods are of little use due to the rising strength of the strong interaction, and so nucleon structure must be described using phenomenological models. Form factors can be used to describe nucleon structure, and these provide an important test for nucleon models, which should be able to reproduce observed form factor behaviour. Measurements of the neutron electric form factor suffer from a number of difficulties including nuclear binding effects and the small size of electric form factor in comparison to the magnetic form factor, leaving the uncertainty on existing

measurements large.

The development of polarised electron sources brought with it the possibility of improved measurement methods. The scattering of polarised electron beams off neutron targets results in the electric form factor appearing in an interference term with the larger magnetic form factor in the recoil neutron polarisation, allowing a determination of  $G_E^n$  by analysis of the neutron polarisation components, and several experiments using such methods have been proposed. One such measurement, using the MAMI-B electron accelerator facility at the University of Mainz's Institut für Kernphysik, took place recently, and is described in this thesis.

# Chapter 2

## Theory and Review

### 2.1 The Neutron

In 1930 Bothe and Becker discovered a highly penetrating form of radiation resulting from the bombardment of Be with  $\alpha$  particles. This radiation was observed to knock protons out of a paraffin target, and by considering the kinematics of this collision, Chadwick provided the most convincing explanation, namely that the radiation was a neutral particle of mass similar to the proton. The existence of a neutral particle in the nucleus successfully accounted for the observed nuclear properties at that time. The photo-disintegration of the Deuteron allowed a more precise determination of the neutron mass, by comparing the masses of D and H and taking into account the binding energy of Deuterium. The neutron is slightly heavier than the proton, with a mass  $m_n = (939.56563 \pm 0.00028)MeV/c^2$  [1]

The original determination of neutron charge was made by considering the ionisation resulting from a neutron's passage through a cloud chamber which gave an upper limit on the neutron charge of  $\sim \frac{1}{700}q^e$  where  $q^e$  is the electron charge. More recent measurements based on the degree of deflection of a neutron on passing through an electric field [2] give a neutron charge of  $(1.5 \pm 2.2) \times 10^{-20}q^p$

where  $q^p$  is the proton charge.

The neutron is heavier than the combined mass of the proton and electron, and is unstable, decaying to  $p + e^- + \bar{\nu}_e$ . Determination of the neutron lifetime is made by observing coincident decay products from a beam of neutrons from a reactor (e.g. [3]). The accepted mean lifetime is  $\tau = (887.0 \pm 2.0)$ seconds [1].

The first accurate measurement of the neutron's magnetic moment was made by Alvarez and Bloch [4], by finding the magnetic field frequency which was in resonance with the Larmor frequency  $\omega_0$  after application of a constant field  $H_0$ , the resonance point being determined by detecting a resulting change in polarisation, and hence passage through a polariser/analyser combination, of a neutron beam. A more accurate recent measurement was performed by Greene [5] in which the ratio  $\frac{\mu_p}{\mu_n}$  was determined by a similar method and yielded the result  $\mu_n = -1.91304184 \pm 0.00000088\mu_N$ .

## 2.2 Form Factors

A form factor represents the spatial distribution of an object, and modifies the scattering cross-section from that of a point charge. In the simple case of scattering from a charge distribution, each element of charge will contribute to the total scattering with different phase shifts. The total scattering cross-section becomes

$$\left(\frac{d\sigma}{d\Omega}\right) = |F(q^2)| \times \left(\frac{d\sigma}{d\Omega}\right)_{Mott} \quad (2.1)$$

where  $F$  is the Form Factor, defined as

$$F(q^2) = \int \rho(\mathbf{r}) e^{i\mathbf{q}\cdot\mathbf{r}} d^3\mathbf{r} \quad (2.2)$$

Here  $q$  is the momentum transfer and  $\rho$  is the charge density.  $F$  is the Fourier transform of the charge distribution, and so performing the inverse transformation allows one to obtain  $\rho$  from a measurement of the differential cross-section.

The scattering of point-like particles such as electrons from a spinless target can be described by the Mott cross section. This takes the form

$$\left(\frac{d\sigma}{d\Omega}\right)_{Mott} = \frac{Z^2 \alpha^2 \cos^2(\frac{\theta}{2})}{4E^2 \sin^4(\frac{\theta}{2}) [1 + (\frac{2E}{M}) \sin^2(\frac{\theta}{2})]} \quad (2.3)$$

where  $Z$  is the nuclear charge,  $\theta$  is the scattered electron angle and  $E$  is the incident electron energy. Here the cosine term in the numerator is due to the electron spin, and the second term in the denominator accounts for the recoil of the target. The remaining terms are essentially those of the classical Rutherford scattering formula.

For scattering from nucleons the expression takes the following form:

$$\left(\frac{d\sigma}{d\Omega}\right) = \left(\frac{d\sigma}{d\Omega}\right)_{Mott} \times \{F_1^2 + \tau [2(F_1 + \mu F_2)^2 \tan^2(\frac{\theta}{2}) + \mu^2 F_2^2]\} \quad (2.4)$$

where

$$\tau = Q^2/4M^2 \quad (2.5)$$

and  $Q^2$  is the square of the 4-momentum transfer. The above expression has 2 Form Factors,  $F_1$  and  $F_2$ , the Dirac and Pauli Form Factors, which are functions of  $Q^2$ .  $\mu$  is the anomalous nucleon magnetic moment, i.e. that differing from the prediction for Dirac point-like particles (e.g. for the neutron  $\mu_{Dirac} = e\hbar/2m_n = 0$ , while  $\mu_{observed} = -1.91\mu_N$ ), and so  $F_2$  can be thought of as representing the contribution to magnetic scattering due to the spatial structure of the nucleon.

It is convenient to introduce form factors  $G_E$  and  $G_M$  which are defined as follows:

$$G_E = F_1 - \tau \mu F_2 \quad (2.6)$$

$$G_M = F_1 + \mu F_2 \quad (2.7)$$

These are the Sachs Form Factors, and simplify the scattering cross-section formula in that no cross-terms in  $G_E G_M$  exist. In the limit of zero momentum transfer, these reduce to the charge and magnetic moment respectively. In the

Breit frame of reference, these Form Factors represent the spatial distributions of charge and magnetic moment.

The cross-section can now be written in the form

$$\left(\frac{d\sigma}{d\Omega}\right) = \left(\frac{d\sigma}{d\Omega}\right)_{Mott} \times \left\{ \left( \frac{G_E^2 + \tau G_M^2}{1 + \tau} + \tau 2G_M^2 \tan^2 \frac{\theta}{2} \right) \right\} \quad (2.8)$$

known as the Rosenbluth formula [6].

The expression for the form factor in equation 2.2 can be expanded in the case of small  $Q^2$  to obtain

$$F = 1 - \frac{Q^2 \langle r^2 \rangle}{6} + \dots \quad (2.9)$$

Hence

$$-\left(\frac{dF}{dQ^2}\right)_{Q^2=0} = \frac{1}{6} \langle r^2 \rangle \quad (2.10)$$

and so the gradient of the form factor as it intercepts  $Q^2 = 0$  gives information about the charge radius.

Scattering experiments where the scattering angle and energy are varied so that  $Q^2$  is fixed, can be carried out and allow  $G_E$  and  $G_M$  to be extracted from a graph of  $\frac{(\frac{d\sigma}{d\Omega})}{(\frac{d\sigma}{d\Omega})_{Mott}}$  vs.  $\tan^2 \frac{\theta}{2}$ . Performing this for various values of  $Q^2$  allows the behaviour of the form factors to be determined. Such experiments have been carried out for the proton, and the results indicate that both  $G_E^p$  and  $G_M^p$  obey the relationship

$$G_E^p(Q^2) = \frac{G_M^p(Q^2)}{\mu_p} = \left(1 + \frac{Q^2}{M_V^2}\right)^{-2} = G_D \quad (2.11)$$

where  $M_V^2 = (0.84 GeV)^2$ .  $G_D$  is known as the dipole form of nucleon form factor.

Transforming the 'dipole' form of  $G^p$ , one obtains exponential charge and magnetic moment distributions  $\rho(r) = \rho_0 \exp(-M_V r)$ , from which the mean square radius is found to be  $r_{rms} = 0.80 fm$ .

## 2.3 Measurements of neutron form factors

In the case of the neutron no free target exists and experiments must be performed on light nuclei such as Deuterium. The main methods which have been used to obtain information on the neutron form factor are : scattering of thermal neutrons from atomic electrons; elastic electron-Deuteron scattering; and quasi-elastic  $D(e, e'n)p$  reactions.

### 2.3.1 Thermal neutron scattering

Information on  $G^n$  at small  $Q^2$  can be obtained by scattering thermal neutrons from atomic electrons [7, 8]. This allows one to determine  $\langle r_n^2 \rangle$  which is related to  $(\frac{\delta G}{\delta Q^2})_{Q^2=0}$  (equation 2.10) and yields the result  $\langle r_n^2 \rangle = (-0.108 \pm 0.006) fm^2$ . This constrains the gradient  $(\frac{dF_1}{dQ^2})_{Q^2=0}$  to be small and indicates that the principal contribution to  $\langle r_n^2 \rangle$  comes from the anomalous magnetic moment.

### 2.3.2 Elastic e-D scattering

Here experiments are performed which measure the structure functions A and B of the Deuteron (in a similar way to that described above). These structure functions are themselves functions of the nucleon form factors, but also of the deuteron wavefunction, and a considerable model-dependence exists on results from such experiments. Platchkov et.al. [9] performed such an experiment in the range  $1 < q^2 < 18 fm^{-2}$ . Here their results and data from earlier experiments are fitted with the Galster parametrisation [10]

$$G_E^n = -\frac{a\mu\tau G_D}{1 + b\tau} \quad (2.12)$$

and are shown in Figure 2.1.  $G_D$  is the dipole form from equation 2.11. The error bars shown in Figure 2.1 are statistical only; in addition there exists

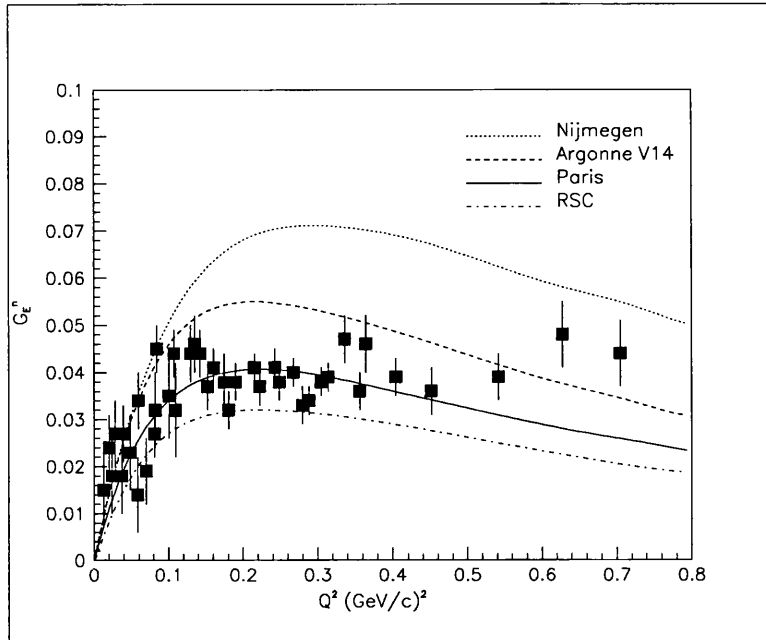


Figure 2.1: Data from ref [13]. The error bars shown are statistical only. Data points shown are obtained by using the Paris potential and result in the best fit line shown (solid line). Using other potentials leads to the curves shown.

a large uncertainty from the choice of potential model used. The points shown are obtained using the Paris potential [11], and the solid line is a best fit to those points. Using other potentials leads to best fits indicated by the other curves, giving a large systematic uncertainty ( $\pm 40\%$ ), although if the fits are constrained by the slope of  $G_E^n$  at  $Q^2 \sim 0$  then only two of the potentials considered, the Paris [11] and Reid Soft Core [12] potentials, result in good fits. The model-dependence remains the dominant uncertainty.

### 2.3.3 Quasi-elastic e-D scattering

Inclusive  $e$ - $D$  inelastic (quasi-elastic) scattering, and exclusive quasi-elastic  $D(e, e'n)$  techniques have been used to extract neutron form factors. Early measurements used the inclusive reaction and deduced the neutron cross-section by assuming

the total quasi-elastic e-D cross-section is equal to the sum of the free e-p and e-n cross sections, with a correction for nuclear effects. Such methods suffer from uncertainty in the correction applied and from large statistical errors (e.g. [13])

Exclusive  $D(e, e'N)N$  measurements where the ratio  $\sigma_n/\sigma_p$  is measured by detecting both n and p channels in the same experiment give results approximately independent of nuclear effects (e.g. [14]). Here the nuclear effects can be checked by comparing free and bound proton cross-sections. The results here suffer from poor statistics and are consistent with  $G_E^n = 0$ . Results for  $G_M^n$  generally support the dipole form (i.e.  $G_M^n = \mu_N G_D$ ). Recent inclusive measurements at high  $Q^2$  [15] suffer from model-dependence and are also consistent with  $G_E^n = 0$ . Recent measurements of  $G_M^n$  by the ratio method (e.g. [16, 17]) also support the dipole form, with small deviations.

## 2.4 Polarised electron beam methods

The use of polarised electron beams opens up new possibilities for the study of nucleon structure. It can be shown [18] that scattering polarised electrons off a polarised neutron target results in an asymmetry with respect to the electron helicity given by

$$\mathcal{A} = -P_e \frac{\alpha G_E^n G_M^n P_x + \beta (G_M^n)^2 P_z}{(G_E^n)^2 + \gamma (G_M^n)^2} \quad (2.13)$$

where  $P_x$  and  $P_z$  are the initial neutron polarisations perpendicular and parallel to the momentum transfer.  $\alpha, \beta$  and  $\gamma$  are kinematical factors and  $P_e$  is the incident electron beam polarisation.

Alternatively one can perform the experiment on an unpolarised target and measure the recoil polarisation of the neutron. In this case the recoil polarisation components are given by [19]

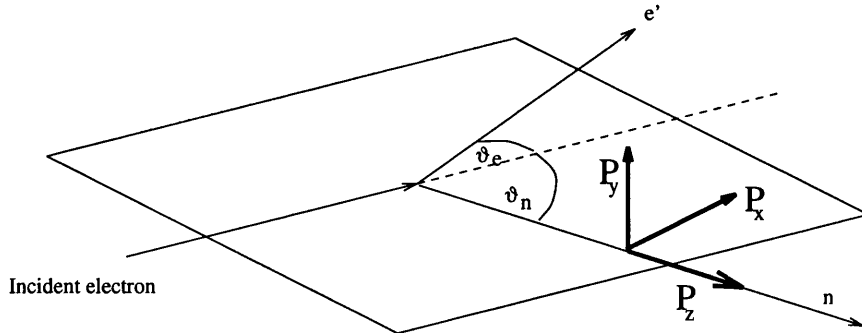


Figure 2.2: Electron-neutron scattering and the recoil neutron polarisation components.

$$P_x = -P_e \frac{2G_E G_M \sqrt{\tau(1+\tau)} \tan \theta_e/2}{G_E^2 + \tau G_M^2 (1 + 2(1+\tau)) \tan^2 \theta_e/2} \quad (2.14)$$

$$P_y = 0 \quad (2.15)$$

$$P_z = P_e \frac{2G_M^2 \tau \sqrt{1+\tau + (1+\tau)^2 \tan^2 \theta_e/2} \tan \theta/2}{G_E^2 + \tau G_M^2 (1 + 2(1+\tau)) \tan^2 \theta_e/2} \quad (2.16)$$

where the  $x, y$  and  $z$  components are defined as in Figure 2.2.  $\tau$  is a kinematical factor,  $\theta_e$  is the scattered electron angle and  $P_e$  is the initial electron beam polarisation.

Here  $G_E^n$  appears in the (transverse)  $P_x$  component ‘magnified’ by the larger  $G_M^n$  component. This allows a measurement of  $G_E$  by measuring the transverse polarisation component of the neutron following scattering from polarised electrons, and assuming the magnetic form factor  $G_M$  is known.

Methods of measuring the polarisation components of the neutron are discussed in Chapter 4.

## 2.5 Nuclear Binding Effects

The absence of a free neutron target means that experiments must be performed on light nuclei. Both the above methods have been used at Mainz in the A3

collaboration: using a polarised  ${}^3\vec{H}e$  target and measuring the asymmetry with respect to the electron helicity, and using a  ${}^2H$  target (unpolarised) in which the polarisation of the final state neutron is determined. In both cases quasi-elastic scattering off the neutron occurs. In polarised  ${}^3\vec{H}e$ , the unpaired neutron possesses most of the nuclear spin and so to a good approximation can be regarded as a polarised neutron target. The two methods, using different nuclear targets, will provide complementary information on the neutron form factors and will indicate any nuclear dependence of the methods.

Small-scale versions of both the full  ${}^3\vec{H}e$  and  ${}^2H$  A3 experiments were carried out, with limited statistics, in 1992 [20, 21]. Results from [20], from a  ${}^2H$  experiment [33] and from several inclusive  ${}^3\vec{H}e(\vec{e}, e')$  experiments [34, 35] are shown in Figure 2.3.

The effects of nuclear binding on the two methods must be considered. Arenhövel [22] investigated theoretically the  $D(\vec{e}, e'\vec{n})$  reaction and found that in quasi-free kinematics the polarisation component  $P_x$  is essentially insensitive to the effects of Final State Interactions (FSI), Meson Exchange Currents (MEC) and isobar configurations. Laget [23] investigated both the  $D(\vec{e}, e'\vec{n})$  and  ${}^3\vec{H}e(\vec{e}, e'n)$  reactions and concluded that the spin observables in those (quasi-free) reactions were essentially the same as those for free neutron scattering. Corrections due to FSI and MEC above  $Q^2 = 0.3(GeV/c)^2$  were found to be small.

These predictions were tested in an earlier A3 experiment [24] in which the polarisation transfer to the proton bound in Deuterium was compared to that to the free proton in Hydrogen. The polarisation transfers were found to be the same, within the experimental error of the experiment ( $\sim 10\%$ ), when close to parallel kinematics were selected, in agreement with the theoretical calculations. This allows a determination of  $G_E^n$  in the reaction  $D(\vec{e}, e'\vec{n})$  to be made with confidence.

## 2.6 Comparison of experiment and theory

The interaction of quarks is described by the theory of QCD (Quantum Chromodynamics), of which the property of asymptotic freedom allows perturbation calculations to be performed to describe high-energy behaviour. These techniques are unsuitable at lower energies, e.g. those involving the nucleon system.

Vector Meson Dominance (VMD) models have been used to describe nucleon interactions at lower energies. Here the virtual photon couples with the nucleon via a strongly-interacting meson. Such models lead to form factors taking the form

$$G = \sum_i \frac{g_i}{(1 + \frac{q^2}{M_i^2})} \quad (2.17)$$

where  $i$  sums over meson states and  $g_i$  are their coupling strengths.

Early scattering experiments indicated that the proton electric and magnetic form factors were well described by the dipole form (equation 2.11). Data for  $G_M^n$ , although less precise, also supported this expression and the relationships in equation 2.11, while most early data on the neutron electric form factor were consistent with  $G_E^n = 0$ , although the slope of  $G_E^n$  at  $q^2 \sim 0$  at least indicated a non-zero value. Later data were described by several forms of parametrisation, e.g.  $G_E = \frac{\mu N \tau}{1+4\tau}$ ,  $G_E^n = -\tau G_M^n$  (i.e. implying  $F_1 = 0$  everywhere), and the ‘Galster’ parametrisation of 2.12.

Lung et.al. [15] compare their recent measurement at high  $Q^2$  with previous data and several theoretical models, including a dispersion theory model [25], a ‘hybrid’ VMD-pQCD model [26], a constituent quark model [28] and a QCD sum-rule model [29]. None of these are able to reproduce both neutron form factors, however. The data of [15] at high  $Q^2$  appear to rule out the models of [26] and [28].

Eden et al. [33] compare their result and other recent measurements with

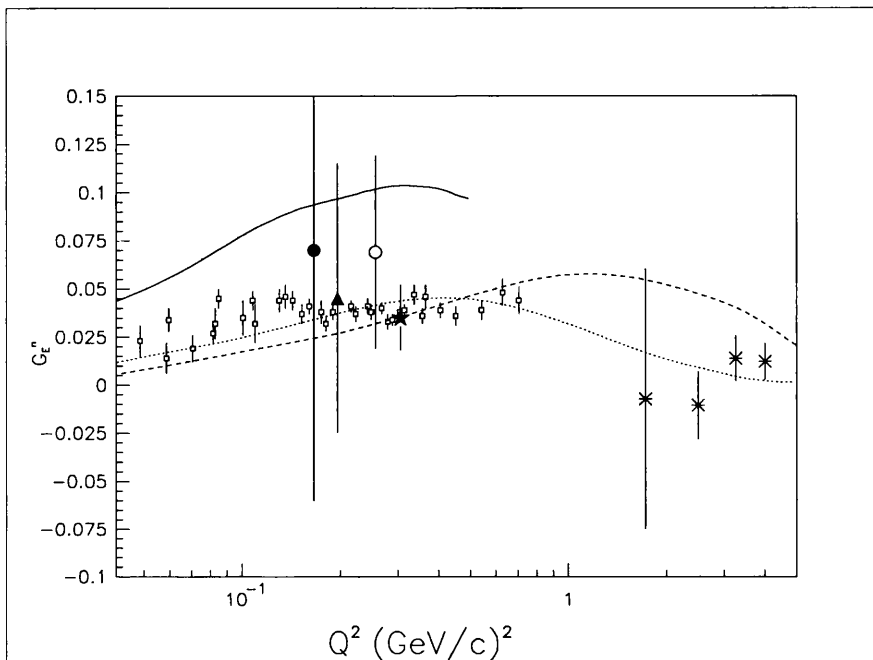


Figure 2.3: Data from Platchkov [9] (open squares), Jones-Woodward [35] (filled circle), Thompson [34] (triangle), Eden [33] (open circle), Meyerhoff [20] (star) and Lung [15] (asterisks). Theoretical curves of Gorski [31] (solid), Cardarelli [32] (dotted) and Gari and Krümpelmann [27] (dashed) are shown. The data points of Platchkov are subject to an additional large systematic uncertainty (see text).

several models including a revised version of Gari and Krümpelmann's model [27] which predicts a significant strange quark content of the neutron and is more consistent with the experimental data. This and the curves of the constituent quark model of Cardarelli et al. [32] and the model of Gorski et al. [31] are shown in Figure 2.3.

More precise measurements of neutron form factors performed recently or taking place in the near future, including those in Mainz, will provide important tests of these theoretical predictions.

# Chapter 3

## Experimental Apparatus

This chapter describes the components of the experimental setup of the  $G_E^n$  measurement. The general set-up is shown in Figure 3.1. A longitudinally polarised electron beam of energy around 855 MeV enters the experimental hall and is incident on a liquid deuterium target. The electrons scattered from the target are detected in an array of 256 lead-glass blocks centered at angle of  $49^\circ$  with respect to the beamline, and the recoil neutrons are detected by a nuclear reaction in a wall of 24 plastic scintillator blocks (the N1 wall), centred at an angle of around  $52^\circ$ . The neutron can then scatter out of the N1 wall and be detected again in a second larger wall of 64 plastic scintillator blocks (the N2 wall). A thin layer of plastic scintillator in front of each polarimeter wall acts as a ‘veto’ detector to discriminate against charged particles. (For clarity these have been omitted from Figure 3.1). The segmented nature of the N1 and lead-glass detectors allows the angle of scattering of the neutron and electron to be determined. This, in combination with neutron time-of-flight information, makes it possible to select quasi-elastic scattering events, i.e. events where the electron has effectively scattered off the neutron alone in the deuterium nucleus.

As described in Chapter 4, the spins of the incident neutrons affect their

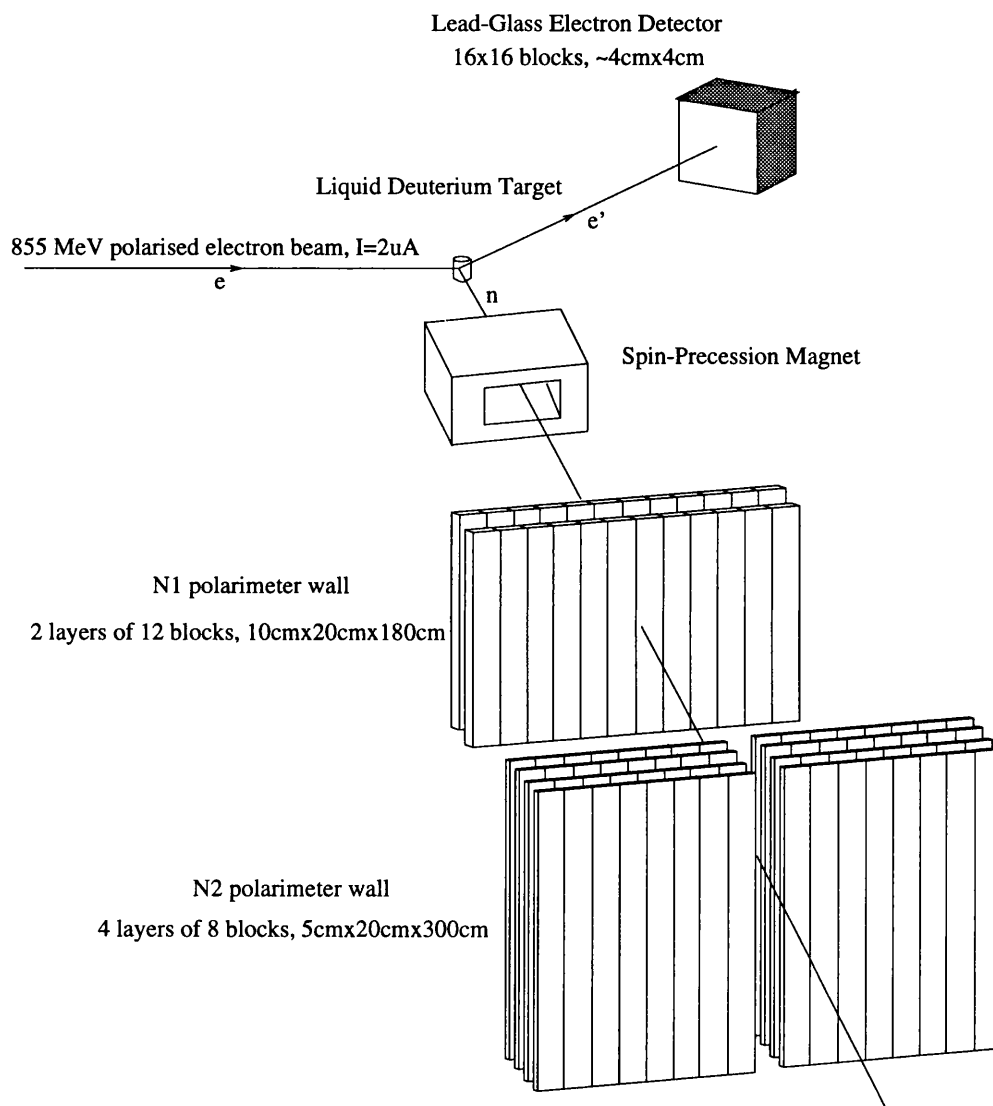


Figure 3.1: The experimental set-up

distribution after scattering, such that a transverse neutron polarisation will lead to an asymmetry in the distribution of neutrons detected in the N2 wall. By observing the distribution of neutrons in the N2 wall, the asymmetry, and hence the incident polarisation, can be calculated.

A magnet, which provides a vertical magnetic field integral of up to  $\sim 1.5Tm$ , is situated between the target and the N1 wall. The magnetic field is sufficient to precess the neutron spin by up to  $\pm 90^\circ$ . This allows a measurement of the  $P_z$  component (see equations 2.14-2.16), and hence a calibration of the polarimeter, to be carried out.

The following sections describe the major components of the system. The neutron polarimeter is discussed in more detail in Chapter 4.

### 3.1 The Polarised Electron Source

A source of polarised electrons is obtained by illuminating a photocathode of Gallium Arsenide with a circularly polarised laser beam, the laser frequency being selected to match the energy gap between the valence and conduction bands of the GaAs crystal. The polarisation of the laser beam allows only transitions with  $\Delta m = \pm 1$ , (for left- and right-circularly polarised light) (Figure 3.2), and so the electrons in the conduction band will have preferential spin directions: that is they will be polarised. Switching the laser polarisation direction reverses the electron polarisation.

The relative intensities of transitions 1 and 2 in Figure 3.2 are 3 to 1 - this makes possible an electron polarisation of 50%. In practice, polarisations of 30% are achieved, due to depolarisation in the electron emission process.

The addition of Phosphorous to the crystal increases the band-gap (to around 1.9 eV) and contributes to a longer crystal lifetime. A flash-lamp pumped dye

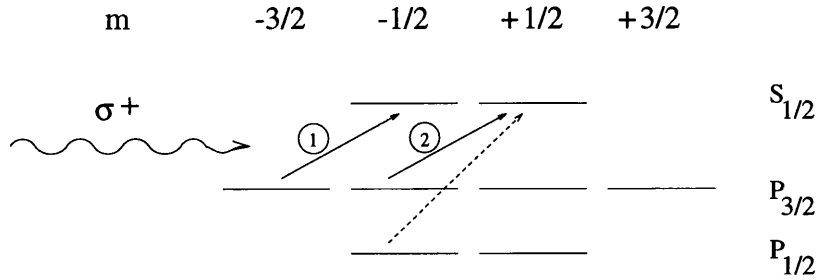


Figure 3.2: Band structure of GaAs

laser tuned to 643nm gives the required photon energy for polarised electron emission from the GaAsP crystal.

The use of a ‘strained’ GaAs crystal allows theoretical polarisations of 100% to be attained, by increasing the separation of the  $P_{3/2}$  levels and using a suitably tuned laser. In practice, polarisations of  $\sim 70\%$  are possible. The beam polarisation direction is controlled by a random pulser operating at 1Hz which results in a 50% probability of changing helicity each second.

### 3.2 The Electron Accelerator

The electrons emitted from the crystal are then accelerated up to an energy of 100keV, and pass through a spin-rotator (see section 3.3) before entering a linear accelerator where they reach an energy of 3.5 MeV. The beam is then directed into the first of three Race-Track Microtron (RTM) stages. (Figure 3.3). In each RTM stage the electron is accelerated in a LINAC , and by means of two dipole magnets the beam is repeatedly directed through the LINAC, each time increasing its energy. At the end of the third microtron stage (RTM3) the electrons can have an energy of up to 855 MeV. The beam is then extracted from RTM3 and can be directed into one of several experimental halls.

MAMI (the Mainzer Microtron) [36] can provide currents of up to  $100\mu\text{A}$  with a 100% duty factor. With a polarised source, currents of up to  $10\mu\text{A}$  with a

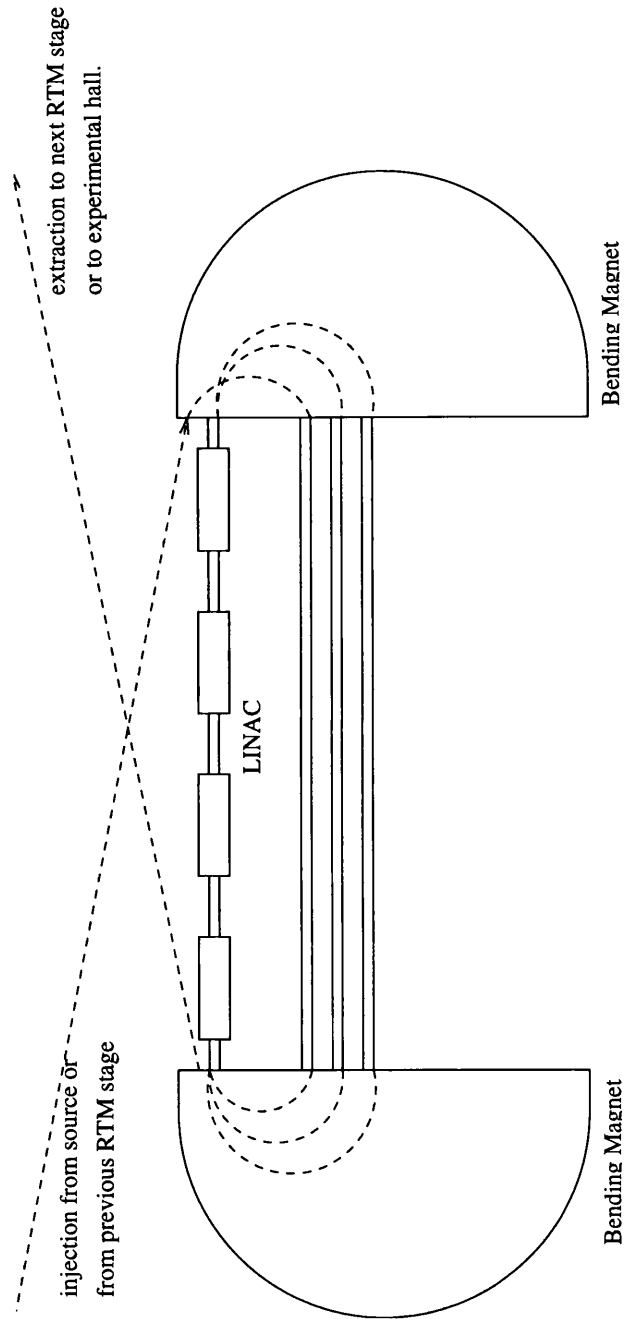


Figure 3.3: The Race-Track Microtron

polarisation of  $\sim 0.35$  are possible from GaAsP, and using a ‘strained’ GaAs crystal, currents of up to  $3\mu\text{A}$  at  $P_e = 0.7$  are possible. Throughout the experiment, the latter combination was used, the lower currents being more suitable for the target and detector system.

### 3.3 The Spin-rotator.

During its travel through the three RTM stages, the electron beam is subject to bending by magnetic fields, which also precesses the spin of the electron. The spin, however, precesses faster than the electron momentum by a factor  $(1 + \frac{\gamma(g-2)}{2})$  [44] (where  $g$  is the  $g$ -factor of the electron), and can thus result in a depolarisation of the electron beam at the extraction point. In order to counteract this, the beam is passed through a spin-rotator (Figure 3.4) before entering MAMI. The spin-rotator allows the spin direction of the electron to be adjusted, in order that the beam extracted from MAMI has optimal longitudinal polarisation.

The spin-rotator [37] consists of two Toroidal Condensers and four sets of double solenoids. On passing through a toroidal condenser, the electron undergoes electrostatic deflection of  $108^\circ$ . In the non-relativistic approximation, the electron spin direction will be unaffected by this deflection, so a deflection of  $90^\circ$  in the first condenser would result in a spin direction transverse to the electron momentum; with electrons of energy  $100\text{keV}$ , a deflection of  $108^\circ$  is necessary for a resultant transverse polarisation.

The solenoids generate magnetic fields in the direction of electron momentum and hence transverse to the electron’s spin, and so the azimuthal angle of spin  $\phi$  can be rotated as required. The electron then passes through a second condenser, allowing the polar angle  $\theta$  to be chosen. Finally two more double solenoids allow the desired azimuthal angle to be selected.

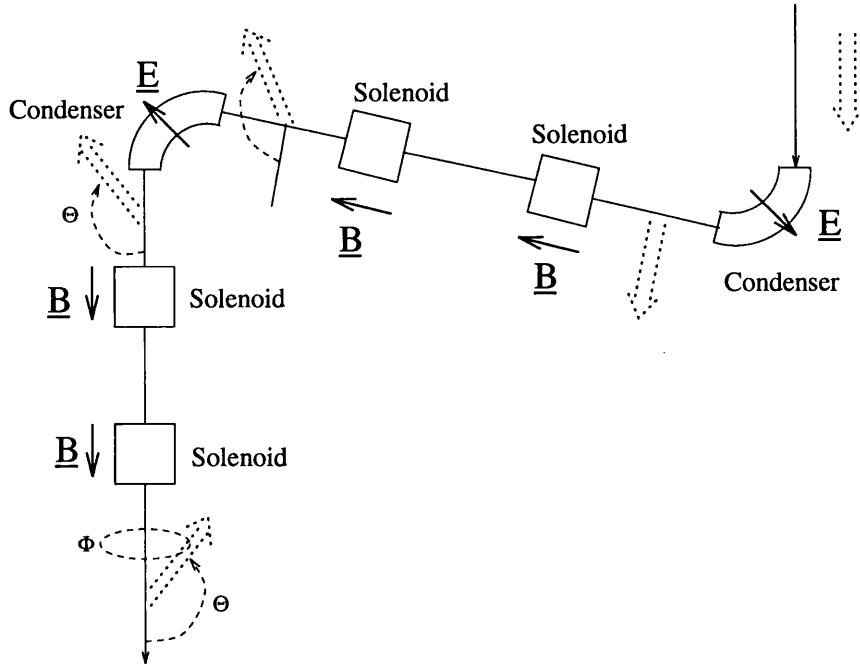


Figure 3.4: The Spin Rotator

The spin-rotator, then, allows the electron spin to be aligned such that on leaving MAMI the beam polarisation is longitudinal.

### 3.4 Electron Polarimeters

Although the measured value of  $G_E^n$  is independent of the electron polarisation, it is important to have a measurement of the beam polarisation to ensure that it is stable and as high as possible. For this purpose, several electron polarimeters are used at various stages during the acceleration and transport of the beam.

A Mott-Polarimeter is situated in the spin-rotator stage. This relies on an asymmetric scattering of electrons from a spin zero nucleus. The asymmetry in the scattered electron distribution is proportional to the degree of (transverse) polarisation of the electron beam. By selecting the plane in which the electron detectors are placed, both transverse polarisation components can be determined.

After leaving MAMI, the beam polarisation can be measured using a Møller

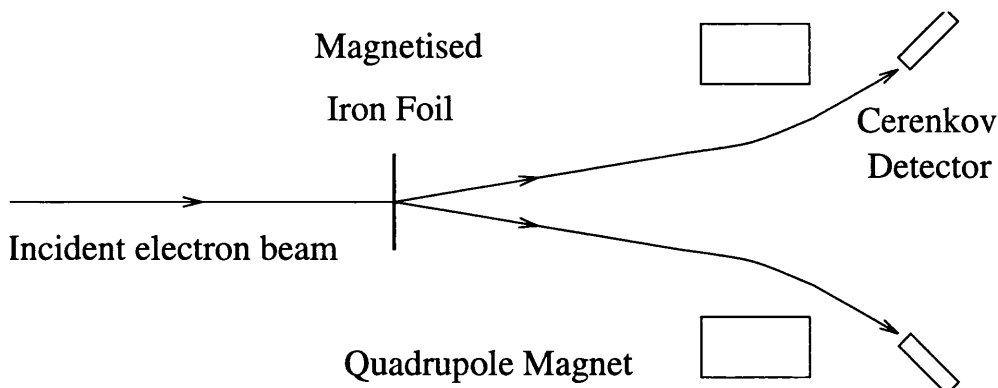


Figure 3.5: The Møller Polarimeter

Polarimeter [38] (Figure 3.5). Here the incident electron is scattered off electrons in a metal foil in which the atomic electrons are polarised due to the application of a magnetic field. The scattered and recoil (target) electrons are detected in coincidence after scattering, and the degree of asymmetry in the scattering cross-section with respect to the incident electron helicity gives a measure of the beam polarisation. By varying the direction of the target polarisation, the different components of beam polarisation can be measured. The quadrupole magnet to the right of the diagram acts as a crude momentum-selector which reduces background from the competing Mott scattering, and eases the detection process by increasing the scattering angle.

Both the above methods interfere with the electron beam and so cannot be used as a continuous monitor of polarisation. An 'online' monitor can be achieved using a Compton Polarimeter. This relies on the asymmetric scattering of polarised photons from polarised target electrons. The polarimeter is situated downstream of the target, the polarised photons originating as bremsstrahlung at the target. The scattered photons are detected in one of two NaI detectors situated behind the target foil.

### 3.5 The Liquid Deuterium Target.

The target consists of a cell of Havar foil of diameter 5cm filled with liquid deuterium and surrounded by a vacuum. Liquefaction is performed by a standard commercial Gifford-MacMahon refrigerator which can achieve temperatures down to 10K through heat exchange with gaseous Helium. Temperature dependent resistors monitor the temperature and a heating resistor maintains the target temperature as required.

### 3.6 The Electron Detector.

The scattered electrons are detected in an array of 256 lead-glass blocks, covering a solid angle of 100 mSr and centred at a scattering angle of  $\sim 49$  degrees. The lead-glass generates Čerenkov radiation when charged particles in the glass travel faster than the speed of light in the glass. An electron entering the lead-glass generates an electromagnetic shower of photons and electrons, the electrons generating Čerenkov light which can be detected in photomultiplier tubes situated at the back of each block. The electromagnetic shower can extend over several of the lead-glass blocks, hence several PM tubes will detect a signal. By using the pulse height information from neighbouring blocks, the position resolution can be improved over that which is possible from only the 4cm x 4cm block dimensions. A resolution of about 7mm can be achieved, corresponding to an angular resolution of  $< \sim 0.3^\circ$ . The energy resolution of the array is relatively poor,  $\sim 20\%$  (FWHM), but is sufficient to reject most inelastic scattering events. An accurate determination of the electron energy is unnecessary for a reconstruction of the reaction kinematics.

### 3.7 Data Acquisition System

The layout of the electronics for the experiment is shown in Figure 3.6. Signals from the top and bottom PM tube of each detector are fed into a splitter box, in which the signal is split in two. One branch leads to a discriminator and TDC (time-to-digital converter) unit, providing the 'stop' signal for the relevant TDC, and the other branch to a QDC (charge-to-digital converter) unit.

The top and bottom discriminator signals are then fed into a coincidence unit, the output of which is fed to a 'OR' logic unit, along with signals from other detectors in the same layer. A positive coincidence output from at least one of the detectors in the B or C layers (i.e. the front and back layers of the N1 wall) results in a 'B OR' or 'C OR' signal. A coincidence from any one of the N2 scintillators will result in either an 'N2 left OR' or 'N2 right OR', corresponding to which branch of the N2 wall the signal originated in. All these signals are fed into an MLU (memory look-up) unit and form an input pattern. The MLU is programmed such that desired input patterns will result in an output pattern which will signal the data acquisition process to continue. The input pattern is checked only when the 'strobe' signal is received, at which point the output pattern is set.

The 'strobe' signal originates from the electron detector. The 256 lead-glass blocks are fed into one of sixteen 16-channel discriminators, the outputs of which lead to the individual TDC modules, providing their 'start' signals. Each discriminator module has an 'OR' output, which is set when any one of their 16 outputs is positive. These are all fed into another 16-channel discriminator module, the 'OR' output of which leads to the strobe coincidence.

The pulse heights from each of the lead-glass blocks are also fed into a summing circuit, the output of which, after passing through a discriminator, is also

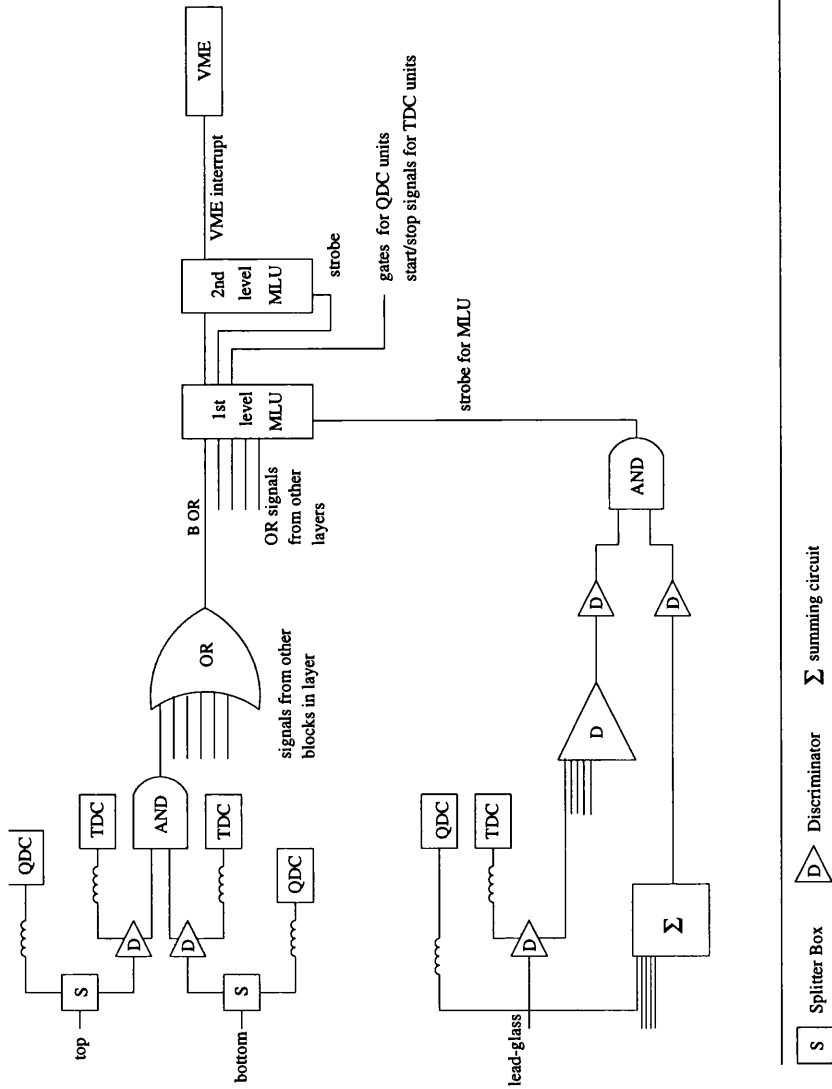


Figure 3.6: Trigger electronics

fed into the strobe coincidence. A positive strobe coincidence then goes on to provide the strobe signal to the MLU. The lead glass 'analogue sum' signal helps to suppress low pulse height background events.

A strobe signal which encounters a suitable MLU input pattern will result in an MLU output pattern which will provide: gates for the QDC modules; the common start signal for the neutron TDCs; the common-stop signal for the electron TDCs; and the 'interrupt' signal to the VME computer, which will then read in the TDC and QDC information from the relevant modules, and disable the trigger system until this is completed. The VME then signals the TDC and QDC units to clear, and the MLU modules to reset, and 're-enables' the data acquisition. The process then repeats.

The TDC and QDC units are FASTBUS standard [39] LeCroy and Philips modules. The discriminator and MLU units are CAMAC standard [40] LeCroy modules which allow remote programming of trigger patterns and discriminator thresholds via the VME [41].

The TDC and QDC information is sent from the VME over an ethernet connection to a Digital Alpha Workstation, where it can be stored on disc and magnetic tape, and sorted to provide an online monitor of the experiment.

# Chapter 4

## The Neutron Polarimeter

### 4.1 Introduction

The neutron polarimeter, a plan view of which is shown in Figure 4.1, consists of two walls of plastic scintillator (NE110), the first wall acting as the analyser, in which the neutron can undergo  $p(n,np)$  scattering, and the second wall detecting the scattered neutron in order to determine its scattering angle. The first wall (N1 wall) is made up of two layers, each layer containing 12 vertical blocks of scintillator measuring 1.8m x 0.2 m x 0.1 m. The N2 wall consists of 8 layers of scintillator, each layer having 8 vertical scintillator blocks measuring 3.0m x 0.2m x 0.05m [42]. In front of each wall are situated veto layers (V1 and V2) consisting of thin (0.01m) overlapping plastic scintillator detectors to discriminate between charged and neutral particles. The ends of each scintillator block are fitted with a light guide and photomultiplier tube (PMT).

Neutrons interact through nuclear reactions with the scintillator material, releasing charged particles which in turn produce photons through the scintillation process. The photons are detected at each end of the block in a PMT, (Figure 4.2), where they are converted into electrical signals, and recorded by the data

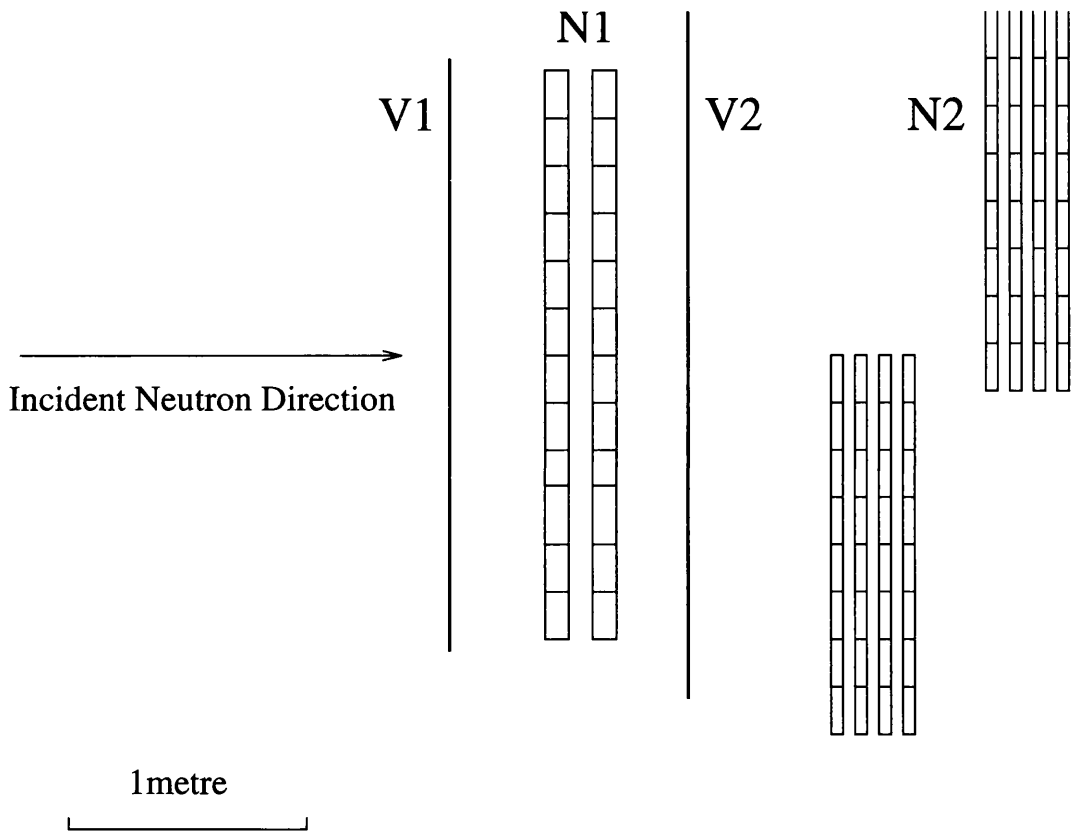


Figure 4.1: A plan view of the neutron polarimeter

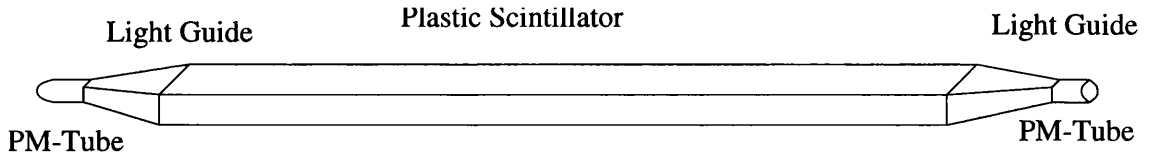


Figure 4.2: A scintillator block

acquisition process.

The position of the interaction along the block can be determined by considering the difference of the time signals from each end of the scintillator. Together with the segmented nature of the array, this lets us determine the coordinate of the interaction in the lab frame. Hence the scattering angles with and the distance travelled by the neutron from the target can be calculated.

The N2 wall is of similar construction to the N1 wall and allows us to determine the angles of scattering between the N1 and N2 walls, and from this to calculate an asymmetry.

The cross-section for neutron-proton scattering is modified in the case of an incident neutron polarisation as follows (Figure 4.3):

$$\sigma(\theta_n, \phi_n) = \sigma_0(\theta_n)[1 + A(T_n, \theta_n)(P_x \sin \phi_n - P_y \cos \phi_n)] \quad (4.1)$$

Here  $\sigma_0$  is the unpolarised  $p(n,np)$  cross-section,  $\theta$  and  $\phi$  are the polar and azimuthal scattering angles,  $P_x$  and  $P_y$  are the two transverse components of neutron polarisation, and  $A$  is the analysing power of the n-p reaction, which is a function of both  $\theta$  and the incident neutron kinetic energy,  $T_n$ . The variation of  $A$  with angle for several neutron kinetic energies is shown in Figure 4.4 [43].

We can form an asymmetry  $A$  which is independent of neutron detection efficiency, and independent of any variation in electron beam luminosity with helicity change [49], by defining the ratio  $R$  to be

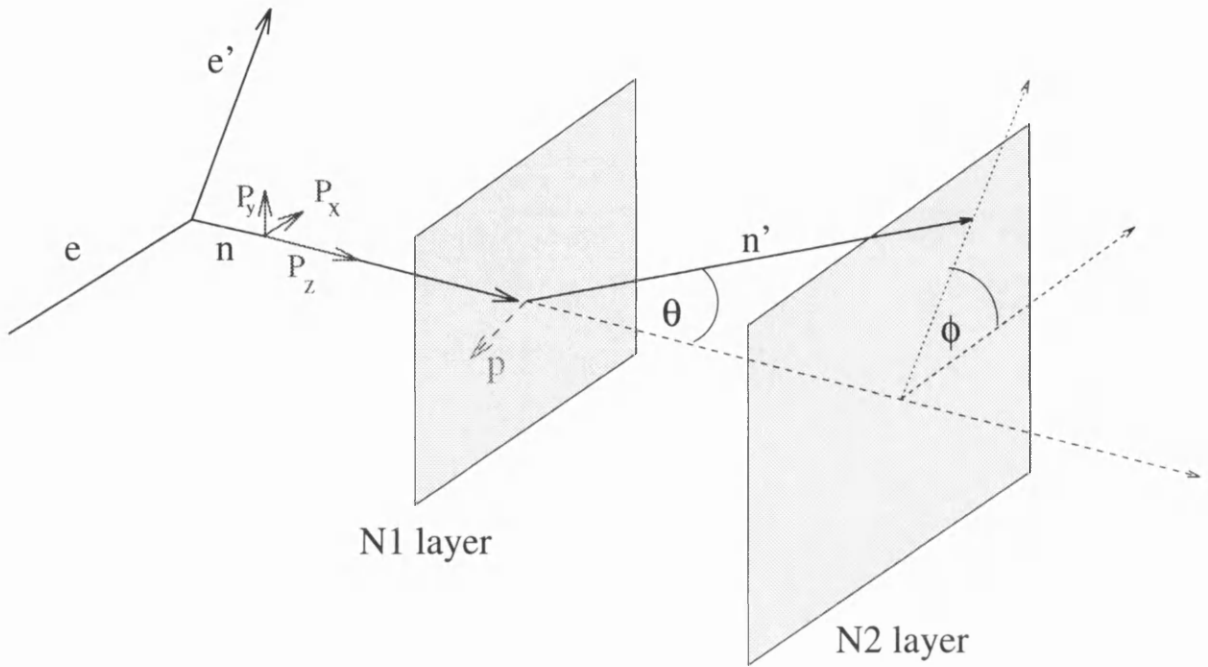


Figure 4.3: Coordinate frame for neutron scattering

$$R = \sqrt{\frac{N^+(\phi) N^-(\phi + 180^\circ)}{N^-(\phi) N^+(\phi + 180^\circ)}} \quad (4.2)$$

Then the asymmetry

$$\mathcal{A} = \frac{1 - R}{1 + R} \quad (4.3)$$

Here  $N^\pm(\phi)$  is the number of counts at a particular azimuthal angle for positive and negative electron helicity.

The measured asymmetry can be written as

$$\mathcal{A} = A(P_x \sin \phi - P_y \cos \phi) \quad (4.4)$$

The analysing power,  $A$ , of the  $p(n, np)$  reaction is well known, and so in principle we can determine the neutron transverse polarisation components from a measurement of the asymmetry.

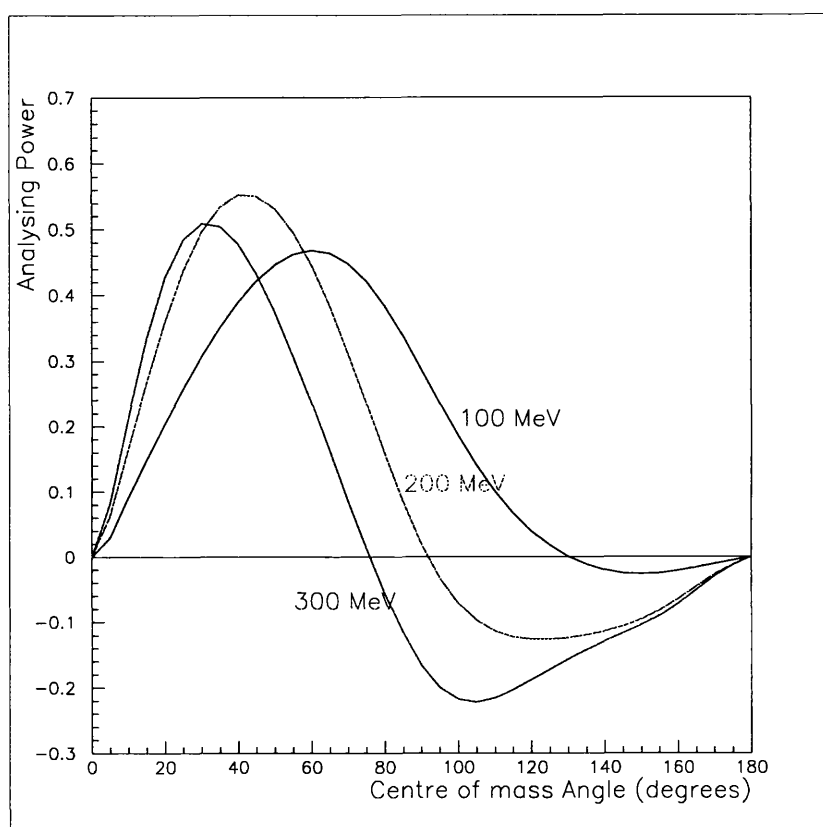


Figure 4.4: Analysing power for n-p scattering

In practice the analysing power of the polarimeter is difficult to calculate. A neutron can be detected in plastic scintillator by undergoing one of several possible reactions. At 200MeV, for example, the n-p reaction occurs only  $\sim 10\%$  of the time, neutron-Carbon reactions dominating the detection process. The neutron-Carbon reaction analysing power is poorly known, but is expected to contribute in some way to the overall analysing power of the polarimeter. Many of the n-C reaction channels result in only a small light output being produced, and so applying a suitable threshold to the detectors removes much of this background. The reaction  $C(n,np)B$ , however, will leave a similar signal in the scintillator as the  $p(n,np)$  reaction, making the two channels difficult to separate. Moreover the  $C(n,np)B$  cross section is around 5 times greater than the  $p(n,np)$  cross-section in the energy range of interest to us.

Calculating the overall analysing power of the polarimeter, then, is difficult. The system thus requires some form of calibration, using, for instance, a neutron beam of known polarisation. A more convenient method, and one that can be performed in Mainz, is to use a neutron spin-precession technique.

## 4.2 The Spin-Precession Method

If the neutron travels through a vertical magnetic field between the target and the N1 wall, then the spin direction of the neutron can be rotated such that the  $P_z$  component, (that which was originally longitudinal, and so to which the polarimeter would not be sensitive) becomes transverse, and hence measurable (Figure 4.5). Then we can measure two asymmetries, under zero and  $90^\circ$  spin-precessions:

$$\mathcal{A}_{zero} = AP_x \sin \phi \quad (4.5)$$

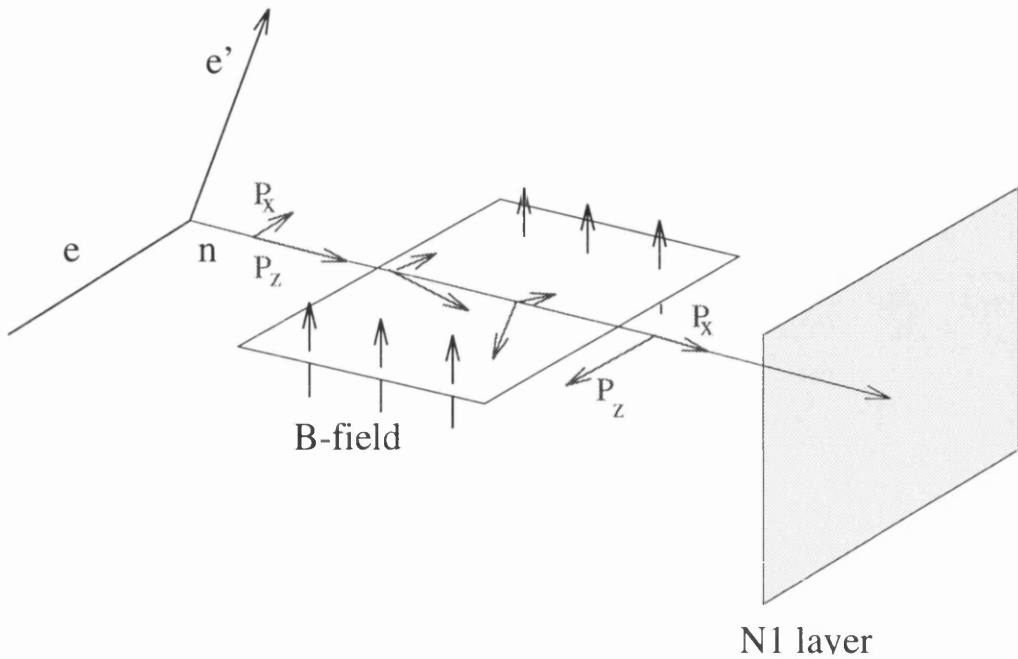


Figure 4.5: The neutron spin-precession method

$$\mathcal{A}_{90} = -AP_z \sin \phi \tag{4.6}$$

assuming  $P_y = 0$  (see equations 2.14-2.16).

Taking the ratio of these we obtain (using equations 2.14 and 2.16)

$$\frac{\mathcal{A}_{zero}}{\mathcal{A}_{90}} = -\frac{P_x}{P_z} = \frac{G_E^n}{G_M^n} \kappa \tag{4.7}$$

where  $\kappa$  is a kinematical factor given by

$$\kappa = \frac{\sqrt{\tau(1+\tau)}}{\tau\sqrt{1+\tau+(1+\tau)^2 \tan^2 \frac{\theta_c}{2}}} \tag{4.8}$$

and

$$\tau = \frac{Q^2}{4m_n^2} \tag{4.9}$$

$Q$  is the 4-momentum transfer, and  $m_n$  is the neutron mass.

Alternatively a series of measurements can be made over a range of spin-precession angles. For an arbitrary precession angle  $\alpha$ , the measured asymmetry is then

$$\mathcal{A}_\alpha = A(P_x \cos \alpha - P_z \sin \alpha) \sin \phi \tag{4.10}$$

Plotting the amplitude of the Asymmetry as a function of  $\alpha$ , we obtain a sinusoidal function, the zero crossing point of which will be given by

$$\tan \alpha = \frac{P_x}{P_z} = -\frac{G_E^n}{G_M^n} \kappa \quad (4.11)$$

The spin-precession technique, then, allows us to measure the ratio  $\frac{G_E^n}{G_M^n}$ , which, assuming the dipole form for the magnetic form factor, gives us  $G_E^n$ .

The precession of a particle's spin in a magnetic field can be described by the BMT equation [44]. In our case where the field direction has only a vertical component, and where the neutron velocity is at right angles to this component, one can obtain:

$$\alpha = \frac{\mu_N g 2\pi}{h} \frac{1}{\beta c} \int B ds \quad (4.12)$$

The field integral necessary for a spin precession of  $90^\circ$  is  $\sim 1.5Tm$ . Field integrals up to this strength are provided by the magnet indicated in Figure 3.1. The magnet consists of two sets of coils surrounding an iron core, arranged to provide an aperture of height  $\sim 200mm$  and width  $\sim 1080mm$  at the target end, widening to a height of  $\sim 400mm$  at the opposite end. The field strengths necessary for a spin-precession of  $\sim 90^\circ$  can be generated by currents of up to 400A, driven by potential differences of up to 200V. Varying the current through the coils varies the field integral, allowing the required range of precession angles to be obtained.

### 4.3 A Monte-Carlo Simulation

In order to investigate the behaviour of the Polarimeter under various experimental conditions, and to study the effectiveness of different data analysis methods, a Monte-Carlo simulation of the polarimeter was carried out.

The software package GEANT [45], developed at CERN, is commonly used for the simulation of nuclear and particle physics experiments. The package provides

useful geometry and tracking routines with which to carry out a simulation, but is intended mainly for use in high-energy physics experiments, and so its ability to model physical processes at energies of around several hundred MeV is limited. In order to provide a realistic simulation of the neutron interactions, the program STANTON [46] was used. This is a neutron detection efficiency code, which models the possible interactions of neutrons in plastic scintillator. The STANTON code gives good agreement with experimentally measured detection efficiencies in the energy range of interest to us [47].

The GEANT and STANTON codes were combined, requiring substantial modification to both packages, to provide a model capable of tracking a neutron through a complex detector geometry. A neutron leaving the target is tracked in GEANT until it enters a scintillator block, when tracking is passed over to STANTON. The STANTON code decides the reaction channel, if any, by which the neutron will interact, and generates the appropriate secondary particles resulting from the reaction, e.g. protons, alpha particles, gammas. These secondary particles are added to a stack and tracked at a later stage by the GEANT code. The neutron, meanwhile, is tracked in STANTON until it disappears in a nuclear reaction, or until it leaves the scintillator, in which case tracking is returned to GEANT.

It is also desirable to simulate the effective analysing power of the polarimeter, and so software routines were written to model the scattering of polarised neutrons by protons, such that an incident beam of polarised neutrons will have a scattered distribution described by equation 4.1.

In order to provide an 'event generator', the neutron at the target is given an initial momentum ('Fermi' momentum) selected from a weighted random distribution of the form shown in Figure 4.6. This distribution was obtained by converting the effective momentum density of reference [48] into a momentum

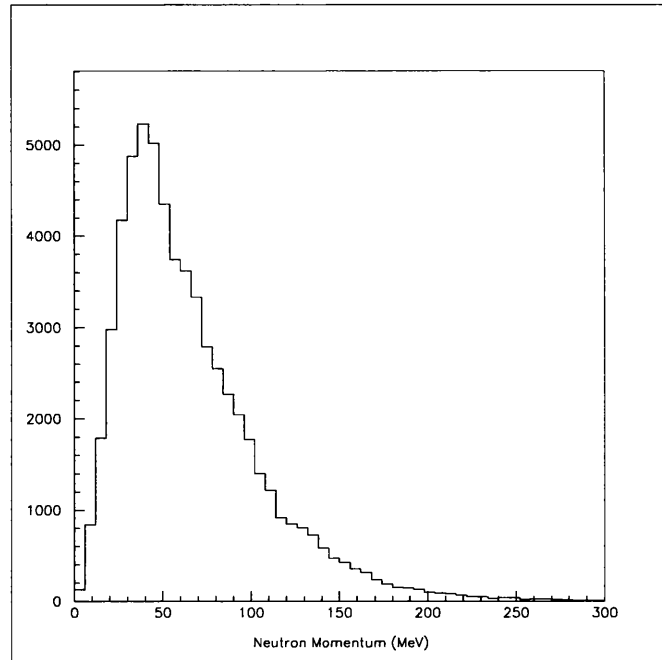


Figure 4.6: Initial neutron momentum distribution

distribution. The neutron was then given a random initial direction.

The electron-neutron scattering can then be simulated by solving the equations of conservation of energy and momentum to give us the outgoing neutron angle and energy as a function of the scattered electron angle. The electron scattering angle was selected from a distribution conforming to that of equation 2.4 (electron scattering cross section from nucleons.)

The model was then used to determine the analysing power attainable under various conditions by firing neutrons of incident polarisation  $P_x = 1$  at the scintillator and measuring the resultant asymmetry. The effectiveness of a polarimeter can be described by the ‘figure of merit’  $M = A^2\epsilon$  where  $A$  is the analysing power and  $\epsilon$  is the efficiency of the polarimeter. The figure of merit obtained after the application of various kinematical cuts was investigated.

The application of a threshold to the scintillator blocks removes much of the background from unwanted n-C interactions. Here a threshold of 5 MeVee

(electron equivalent MeV, i.e. the light which would be produced by an electron of energy 5 MeV) was applied was found to be sufficient to remove most reactions other than the p(n,np) and C(n,np)B channels. Selecting scattered neutrons in the range  $10^\circ - 40^\circ$  gives us scattering events where the analysing power is at its greatest (Figure 4.4), and increases the overall analysing power of the polarimeter.

The separation of the p(n,np) and C(n,np)B reactions presents the most problems. The p(n,np) reaction can be described by two equations corresponding to the conservation of energy and linear momentum respectively:

$$T_n = T_{n'} + T_p \quad (4.13)$$

$$T_p^2 + 2m_p T_p = p_n^2 + p_{n'}^2 - 2p_n p_{n'} \cos \theta_{n'} \quad (4.14)$$

Here  $T_n$  and  $p_n$  are the energy and momentum of the incident neutron,  $T_{n'}$ ,  $T_p$ ,  $p_{n'}$  and  $p_p$  are the kinetic energies and momenta of the scattered neutron and proton, and  $\theta_{n'}$  is the scattered neutron polar angle.

If we define

$$Q_1 = \frac{T_p^2 + 2m_p T_p}{p_n^2 + p_{n'}^2 - 2p_n p_{n'} \cos \theta_{n'}} \quad (4.15)$$

and

$$Q_2 = \frac{T_n}{T_p + T_{n'}} \quad (4.16)$$

then we can select regions of  $Q_1$  and  $Q_2$  around 1.0 to enrich the ratio of p(n,np) to C(n,np)B events and hence increase the analysing power. Typical distributions of  $Q_1$  and  $Q_2$  for p(n,np) only and for all reaction channels are shown in Figure 4.7

The ability to reconstruct the kinematics of the scattering, and hence separate the two competing reactions, is highly dependent on the time resolution of the system. Tables 4.1 to 4.3 summarise the results of the Monte-Carlo simulations,

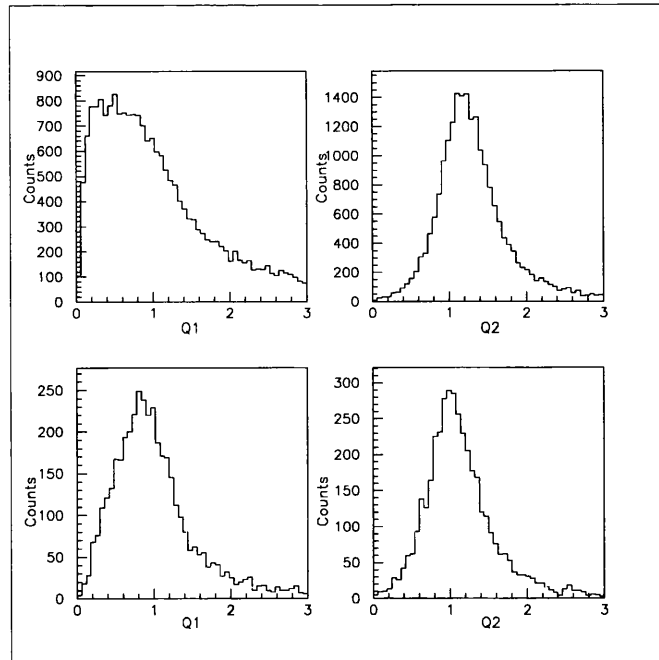


Figure 4.7: Top: the ratios  $Q_1$  and  $Q_2$  for all reaction channels. Bottom: the same ratios for the  $p(n,np)$  channel only.

which were carried out for a range of detector time resolutions: 0.5, 1.0 and 2.0 ns FWHM (Full Width Half Maximum).

An independent simulation was carried out previously in Mainz by A.Frey [21], in which the above parameters were chosen as a means of enriching the  $np/nC$  ratio. The same parameters were chosen here to enable a comparison with the results of [21]. In general the results are in good agreement, with similar analysing powers and figures of merit found under the same conditions.

If we define

$$D = T_p^{\text{measured}} - T_p^{\text{np scattering}} \quad (4.17)$$

(i.e. the difference between the measured proton kinetic energy from pulse height information, and the kinetic energy calculated using the time-of-flight information at the N1 wall, and angular information from the N1 and N2 walls), and use cuts around  $D = 0$  to improve the analysing power, we find that, for the case of a

| Condition |                      |          |         |                 | Asymmetry<br>(%) | $M$<br>( $\times 10^{-5}$ ) |
|-----------|----------------------|----------|---------|-----------------|------------------|-----------------------------|
|           | $\theta_2(^{\circ})$ | $Q_1$    | $Q_2$   | $D(\text{MeV})$ |                  |                             |
| 1         | 10-35                | -        | -       | -               | 13.2             | 5.2                         |
| 2         | 10-35                | 0.6-1.35 | -       | -               | 22.3             | 11.9                        |
| 3         | 10-35                | 0.7-1.2  | -       | -               | 27.0             | 12.4                        |
| 4         | 10-35                | 0.6-1.35 | $< 1.8$ | -               | 22.3             | 10.9                        |
| 5         | 10-35                | 0.7-1.2  | $< 1.4$ | -               | 26.9             | 10.1                        |
| 6         | 10-35                | -        | $< 1.8$ | $-3 < D < 3$    | 31.4             | 8.9                         |
| 7         | 10-35                | -        | $< 1.8$ | $-8 < D < 8$    | 27.3             | 15.7                        |
| 8         | 10-35                | -        | $< 1.8$ | $-12 < D < 12$  | 23.3             | 15.7                        |

Table 4.1: Monte-Carlo results for 0.5ns resolution

| Condition |                      |          |         |                 | Asymmetry<br>(%) | $M$<br>( $\times 10^{-5}$ ) |
|-----------|----------------------|----------|---------|-----------------|------------------|-----------------------------|
|           | $\theta_2(^{\circ})$ | $Q_1$    | $Q_2$   | $D(\text{MeV})$ |                  |                             |
| 1         | 10-35                | -        | -       | -               | 9.4              | 5.0                         |
| 2         | 10-35                | 0.6-1.35 | -       | -               | 19.7             | 8.5                         |
| 3         | 10-35                | 0.7-1.2  | -       | -               | 18.5             | 5.5                         |
| 4         | 10-35                | 0.6-1.35 | $< 1.8$ | -               | 20.8             | 8.2                         |
| 5         | 10-35                | 0.7-1.2  | $< 1.4$ | -               | 23.1             | 6.4                         |
| 6         | 10-35                | -        | $< 1.8$ | $-3 < D < 3$    | 23.2             | 4.2                         |
| 7         | 10-35                | -        | $< 1.8$ | $-8 < D < 8$    | 16.1             | 4.9                         |
| 8         | 10-35                | -        | $< 1.8$ | $-12 < D < 12$  | 16.2             | 7.1                         |

Table 4.2: Monte-Carlo results for 1.0ns resolution

0.5ns time resolution, the figures of merit are improved by up to 50% over those achieved using only the  $Q$  parameters.

With poorer time resolutions, however, the figures of merit are no better than those obtained by using the  $Q$  parameters only. The figures of merit and analysing powers attainable under poorer time resolutions are much smaller, e.g. those with 2.0ns time resolution (Table 4.3) have maximum analysing powers of only  $\sim 17\%$ . The 0.5 and 1.0 ns simulations were carried out primarily for comparison with the results of [21], and used a slightly different detector geometry. The 2.0ns resolution was then carried out with the same detector geometry and timing resolution as in the full-scale experiment. Several choices of  $\theta'_n$  range were used and the optimum range found to be  $10^\circ < \theta'_n < 40^\circ$ . This has the effect of lowering slightly the maximum analysing powers, but increasing the figure of merit. With the 2.0ns resolution simulation, much lower analysing powers are achieved, and are generally obtained with wider cuts on the kinematic variables, optimum  $M$  being found around  $0.1 < Q_1 < 1.4$  and  $Q_2 < 1.8$ , although the difference in  $M$  for similar values of cuts was small. Clearly the polarimeter's performance is strongly dependent on the time resolution, with resolutions of  $\leq \sim 1.0ns$  required to achieve large improvements ( $\sim 300\%$ ) over the situation where no enrichment cuts are applied. For 2.0ns resolution, improvements to  $M$  of  $\sim 50\%$  can still be achieved using enrichment cuts. In the analysis of the experiment which follows (Chapters 5 and 6), a time resolution of  $\sim 2.0ns$  was found, and comparisons with the simulation results are made.

The Monte-Carlo studies described above indicate the optimum methods of data analysis and, by comparing the results with those of the experimental analysis, should confirm that the behaviour of the polarimeter is well understood.

| Condition            |         |       | Asymmetry<br>(%) | $M$<br>( $\times 10^{-5}$ ) |
|----------------------|---------|-------|------------------|-----------------------------|
| $\theta_2(^{\circ})$ | $Q_1$   | $Q_2$ |                  |                             |
| 10-40                | -       | -     | 8.5              | 3.4                         |
| 10-40                | 0.0-2.0 | -     | 10.4             | 4.1                         |
| 10-40                | 0.0-1.8 | -     | 11.0             | 4.3                         |
| 10-40                | 0.0-1.6 | -     | 12.2             | 4.6                         |
| 10-40                | 0.0-1.4 | -     | 13.0             | 4.6                         |
| 10-40                | 0.0-1.2 | -     | 13.9             | 4.4                         |
| 10-40                | 0.1-1.4 | -     | 13.2             | 4.7                         |
| 10-40                | 0.2-1.4 | -     | 12.9             | 4.3                         |
| 10-40                | 0.4-1.4 | -     | 13.0             | 3.9                         |
| 10-40                | 0.6-1.4 | -     | 13.1             | 3.3                         |
| 10-40                | 0.7-1.4 | -     | 13.5             | 3.2                         |
| 10-40                | 0.1-1.4 | < 2.0 | 14.3             | 5.0                         |
| 10-40                | 0.1-1.4 | < 1.8 | 14.7             | 5.1                         |
| 10-40                | 0.1-1.4 | < 1.6 | 15.1             | 4.9                         |
| 10-40                | 0.1-1.4 | < 1.4 | 16.2             | 4.7                         |
| 10-40                | 0.1-1.4 | < 1.2 | 18.5             | 4.5                         |
| 10-40                | 0.1-2.0 | < 1.8 | 11.5             | 4.4                         |
| 10-40                | 0.1-1.8 | < 1.8 | 12.0             | 4.7                         |
| 10-40                | 0.1-1.6 | < 1.8 | 13.3             | 4.9                         |
| 10-40                | 0.1-1.4 | < 1.8 | 14.7             | 5.1                         |
| 10-40                | 0.1-1.2 | < 1.8 | 16.2             | 5.1                         |

Table 4.3: Monte-Carlo results for 2.0ns resolution

## 4.4 A Kinematical Trigger

The trigger electronics described in section 3.7 require that a ‘hit’ is obtained in the lead-glass detector and both the N1 and N2 walls. No demands are made on the positions within the lead-glass and N1 walls in which the hits were recorded. Due to the nature of the e-n scattering, the angles of the outgoing electron and neutron will be related, and so for a given electron angle we will be interested only in neutrons which are scattered at a particular angle, or more correctly a range of angles, owing to the initial Fermi momentum of the neutron which will smear out the angular relationships.

Figure 4.8 shows the distribution of events recorded during an experimental run carried out in the summer of 1994 with an unpolarised beam and a liquid deuterium target. Here large column numbers correspond to forward (i.e. small) angles in each detector. Superimposed on the diagram is the region in which quasi-elastic events will occur, allowing for the initial target neutron momentum. It can be seen that a large proportion of events occur well outside the region of interest to us, particularly at forward angles.

A simple analysis of the data produced the plot on the left of Figure 4.9, showing the measured neutron kinetic energy, measured by time-of-flight, plotted against the electron pulse-height. It can be seen that a large proportion of events have either an electron energy which is too low, corresponding to inelastic e-n scattering (e.g. pion production, delta resonances), or a neutron kinetic energy which is too low (less than  $\sim 100\text{MeV}$ ). As a rough indication of the proportion of ‘good’ events, the data falling within the delineated region were counted and found to make up only  $\sim 17\%$  of the total.

By using several MLU units, it should be possible to design an online trigger which would accept events falling within the delineated region of Figure 4.8. The

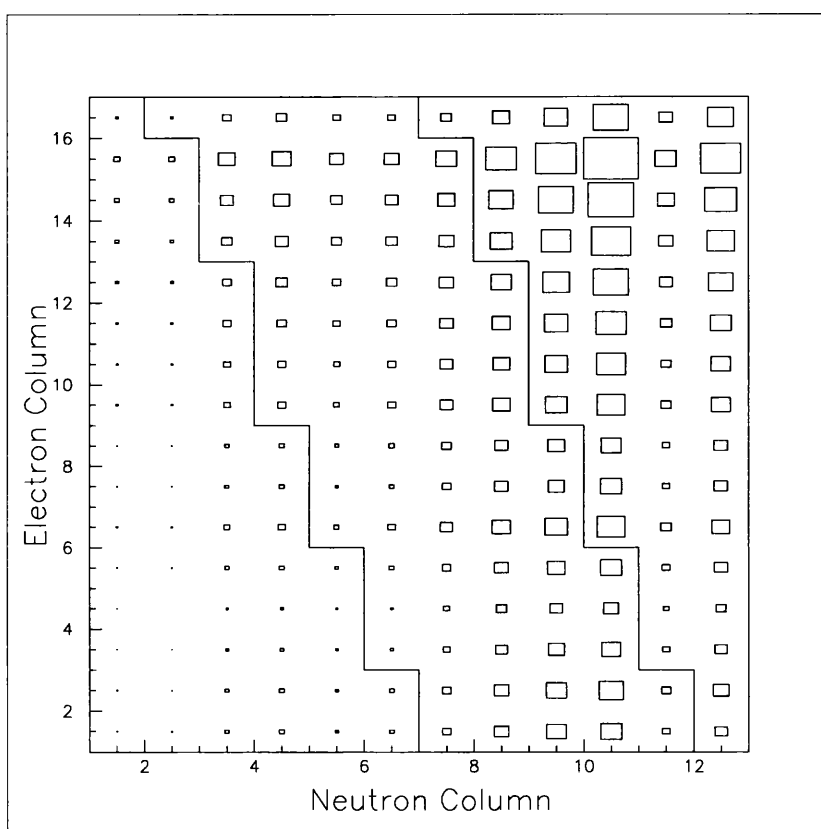


Figure 4.8: Distribution of events: n1 column versus electron column

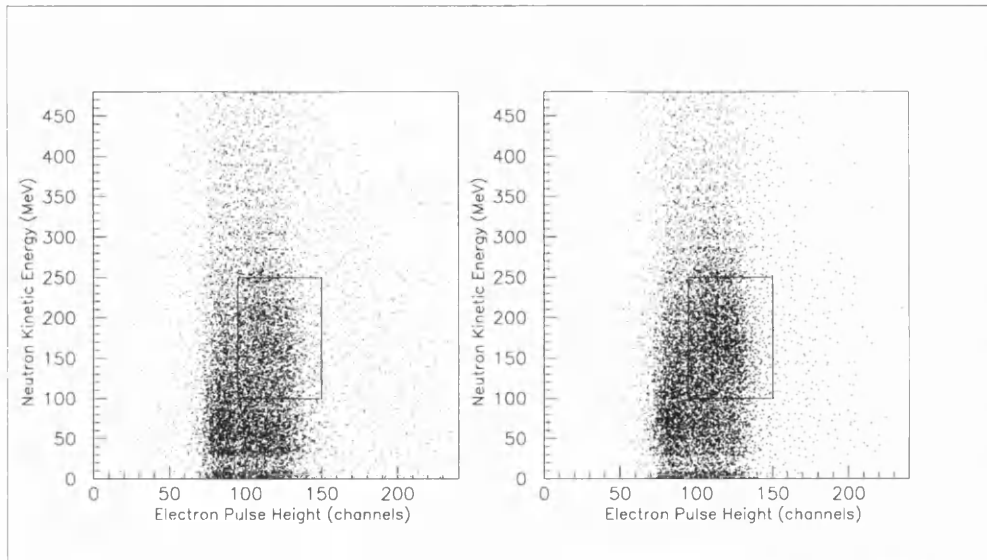


Figure 4.9: Neutron kinetic energy against lead-glass pulse height. Left: without simulated trigger conditions. Right: with simulated trigger conditions.

experimental data were used to simulate the conditions which could be applied in such a trigger, and to investigate the potential improvements which could result.

In order to allow for the spread resulting from the initial Fermi motion of the neutron, for a particular electron angle, i.e. a particular column in the lead-glass detector, the neutron is allowed to fall into any of 5 scintillator blocks around the central angle. The scintillator proton can then proceed to the second layer of the N1 wall, or into adjacent blocks outside the 5-block region, and so the trigger was designed to allow for such events. Monte Carlo studies, however, suggest that only a small proportion of events ( $\sim 5\%$ ) fall into this category. Events where non-adjacent column hits occur in either the N1 wall or the lead-glass detector were also rejected.

The right hand side of Figure 4.9 shows a plot of neutron pulse height versus lead-glass pulse height after the application of these simulated trigger conditions. Here  $\sim 30\%$  of the events fall within the delineated region. Much

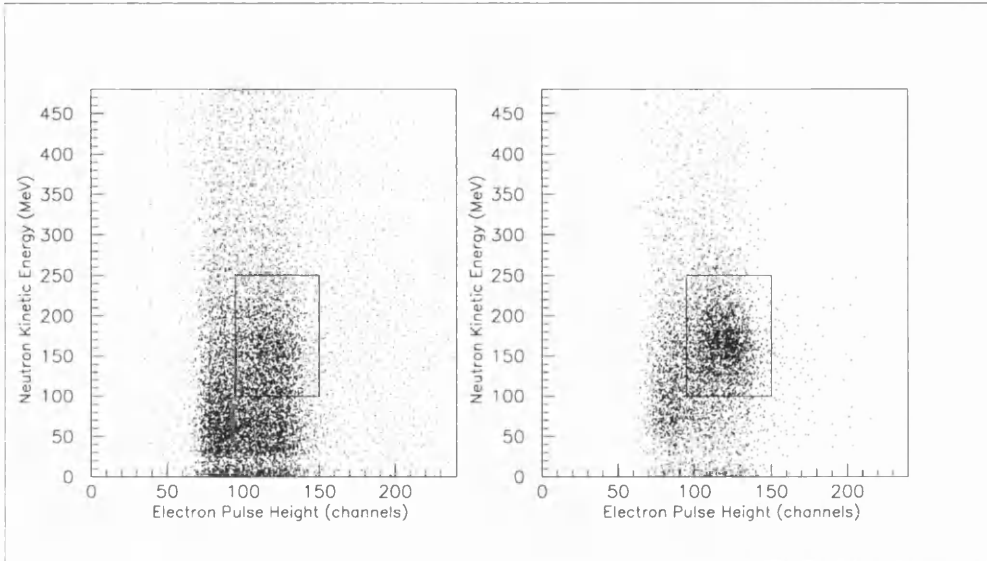


Figure 4.10: Neutron kinetic energy against lead-glass pulse height at forward electron angles. Left: without simulated trigger conditions. Right: with simulated trigger conditions.

of this improvement occurs at forward electron angles - limiting ourselves to the forward five electron columns, for instance, we obtain Figure 4.10. Here 18% of the events fall into the delineated region before the application of the simulated trigger conditions, and 54% after conditions have been applied.

Such conditions, then, should provide a useful reduction in trigger rate by upto a factor 4, and, on the basis of this preliminary analysis, similar conditions were implemented into the trigger of the full experiment. This was achieved by using four 16-bit MLU units. Discriminator signals from the N1 B layer, N1 C layer and lead-glass detector were fed into three separate MLUs, each of which were programmed to give a 4-bit output signal corresponding to the position of the ‘hit’ in the relevant detector group. These were fed into a fourth MLU which interpreted the positions of the hits in the 3 detectors groups, and gave an output signal corresponding to whether or not the event fell within the desired region.

This signal was then fed into the 2nd level MLU of Figure 3.6, where it could be demanded before sending an interrupt signal to the VME.

# Chapter 5

## Data Analysis

The experimental data were taken over the period September 1995 to January 1996, after which the data were analysed.

### 5.1 Neutron Detector Calibrations

#### 5.1.1 Timing Corrections

An important element in the reconstruction of the events is the timing of the system. An accurate knowledge of the relative times of hits in various detectors is required in order to reconstruct the event which has taken place. The time-of-flight is required to select events of interest to us and to determine the kinetic energy of the neutron, and the relative timing of the signals from the ends of each scintillator block is required to reconstruct the position of the interaction, and hence to calculate the relevant scattering angles. As was discussed in Chapter 4, the performance of the polarimeter is highly sensitive to the timing resolution.

In order to reconstruct the kinematics of each event, a knowledge of the time taken for the neutron to reach the polarimeter is required. The time signal recorded by the neutron TDC modules is the difference between the ‘stop’ signal

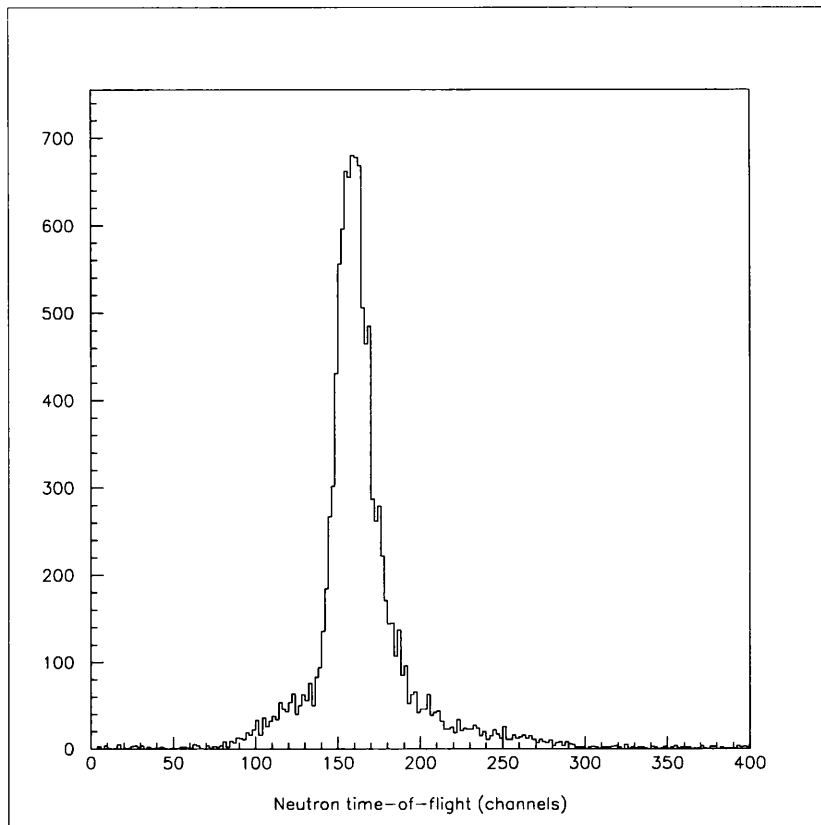


Figure 5.1: A neutron TDC spectrum

and the 'start' signal. The 'stop' signal originates from the corresponding neutron discriminator; the 'start' signal is common to all the neutron TDC modules and originates from the output of the MLU (see Chapter 3).

A typical neutron time-of-flight spectrum is shown in Figure 5.1. The neutron TDCs operate in 'common start' mode, that is a single signal, originating in our case from the lead-glass detector, provides the 'start' signal for all the neutron TDCs. The stop signal is then provided by each individual neutron discriminator. Hence events lying to the right of Figure 5.1 correspond to neutrons which have taken longer to arrive at the detector and so which have lower energies.

The timing of the MLU output is determined by the time of the MLU 'strobe' signal, which comes from a 2-way coincidence between the electron 'OR' signal

and the electron ‘analogue sum’ signal. As discussed in Chapter 3, the analogue sum signal is the later to arrive at the coincidence, and so determines the strobe timing, and hence the neutron TDC ‘start’ timing.

The analogue sum signal will itself vary due to different delays in the lead-glass cables and due to the effects of ‘walk’ in the leading-edge discriminators. One can remove this variation by using a signal which is subject to the same variation, e.g. the lead-glass TDCs. These operate in ‘common stop’ mode, i.e. the start signal is provided by a lead-glass discriminator, and the stop signal is provided by the analogue sum. By adding the contents of a lead-glass TDC to a neutron TDC, we can eliminate the variation due to the analogue sum time.

The electrons are relativistic, and so the time taken for them to reach the lead-glass array will vary only very slightly over the various lead-glass blocks, hence we can say that the electrons provide us with a signal which occurs at a constant point in time. However, the lead-glass TDC signal will also be subject to variation, both from differences in cable delays of the individual blocks and from the ‘walk’ effect. This effect arises due to the variation in pulse height of the input signal, and results in the discriminator being triggered at a time dependent on the pulse height (see Figure 5.2). A large pulse height signal will reach the threshold sooner than a smaller pulse, and so the discriminator output will occur sooner than that for a pulse near the threshold level.

The following correction can be applied to the measured time  $t$  to correct for the leading edge walk effect [51].

$$t' = t + r(1 - \sqrt{\frac{a_0}{a}}) \quad (5.1)$$

where  $a_0$  is the discriminator threshold,  $a$  is the pulse height and  $r$  is the risetime of the pulse. The threshold can be determined by observing the QDC spectrum for the corresponding TDC and noting the lowest channel when that

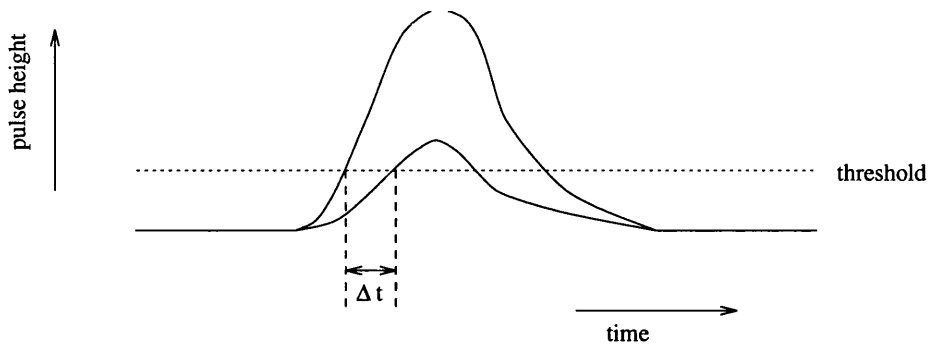


Figure 5.2: The leading-edge walk effect.

TDC has fired. The risetime is more difficult to determine, as the variation in the analogue sum TDC signal masks this. Here we can take advantage of the related  ${}^3\text{He}$  experiment (see Chapter 2), which used essentially the same detector and acquisition system as in the present experiment. There the trigger was made by a signal from an air-Čerenkov detector after passing through a constant fraction discriminator (CFD), and so was not subject to the same leading edge walk effect. Hence any slew visible in the start time of each lead glass TDC will be due to the walk effect in the lead glass discriminators.

The air-Čerenkov detector consists of a focussing mirror and a PM tube. Electrons scattered from the target will emit Čerenkov radiation while passing through the air on their way to the lead-glass detector. The angle at which this radiation is emitted is determined by the electron velocity and the index of refraction of the medium. The focussing mirror is arranged such that the Čerenkov photons will be reflected onto the PMT only if the electron has originated in the target cell, and so the air-Čerenkov signal can be used to cut down background electrons originating in the entrance or exit windows of the target cell. The signal, after passing through a CFD, is incorporated into the strobe coincidence and is arranged so that it arrives last, and hence determines the timing of the system.

By examining  ${}^3\text{He}$  data, the lead-glass risetime can be estimated by observing

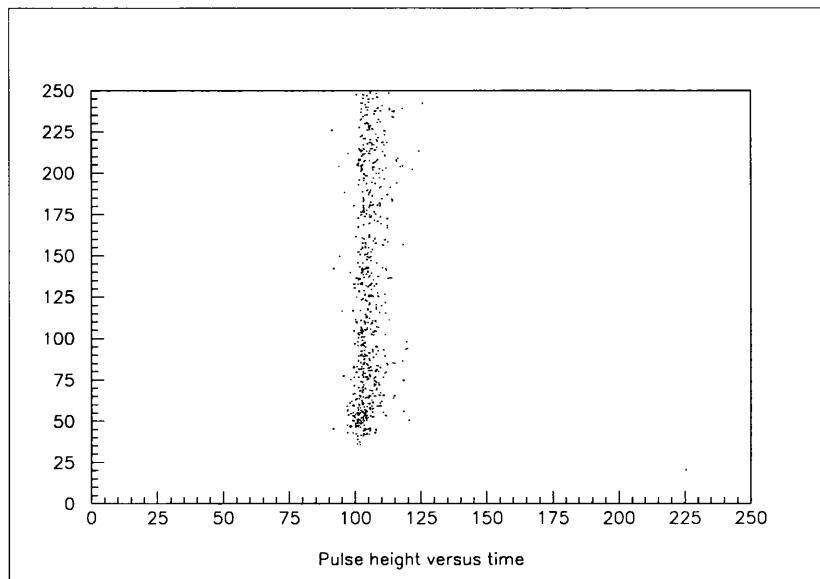


Figure 5.3: The walk effect in a lead-glass TDC.

the variation in its time as a function of its pulse height. Figure 5.3 shows a plot of pulse height versus time for a lead glass block, from which the risetime was estimated to be  $\sim 3ns$ .

The lead-glass TDCs require to be aligned with respect to one another to account for any variations in e.g. cable delays. To do this, the lead-glass TDCs must first be corrected for the variation in the analogue sum stop signal. The analogue sum risetime can be determined in the same way as the lead-glass risetime described above.

A correction for lead-glass and analogue sum walk can then be applied to each lead-glass TDC. The variation in time taken for electrons to reach various parts of the lead-glass detector will be extremely small ( $\ll 25ps$ , the resolution of the electron TDC units), and so it can be assumed that the electron signal gives us a constant reference point in time. The position of the peak for each of the 256 lead-glass TDC spectra, after the application of walk corrections, was noted.

For any one event, the lead-glass block with the largest QDC content was noted, and its TDC content, after application of time corrections, compared to the peak value for that TDC. This difference, representing the deviation from a constant reference time, was subtracted from the neutron TDCs, thereby correcting for any variations due to the lead-glass system.

The neutron TDCs are themselves subject to the leading-edge walk effect, and so the thresholds and risetimes of each detector must be determined. The thresholds are found by demanding that a particular TDC has fired, and noting the lowest non-zero channel in the corresponding QDC spectrum. The risetime is more difficult to determine, as for each neutron TDC we are dealing with both a wide range of flight-times and a range of interaction positions along the block, thus smearing out the effect of walk.

Ideally, a signal of constant time is required, so that the only variation visible will be that of walk. Here the relativistic particles are useful. It may be assumed that these particles arrive at the same time with respect to the time origin. Their range of pulse heights will be much smaller than those from neutrons, but was nevertheless found to be of sufficiently large range to enable the risetime to be determined.

Figure 5.4 , a graph of neutron pulse height versus time, illustrates the walk effect. It can be seen that the smaller pulse heights tend to arrive later due to the longer time required to trigger the 'stop' signal.

If it is assumed that, over the initial rise period of the pulse, that the pulse rises as a quadratic function of time, then one can write

$$t\sqrt{a} = r\sqrt{a_0} \quad (5.2)$$

A graph of  $t$  versus  $\frac{1}{\sqrt{a}}$  will have a gradient proportional to the risetime which can then, using our knowledge of the threshold, be determined.

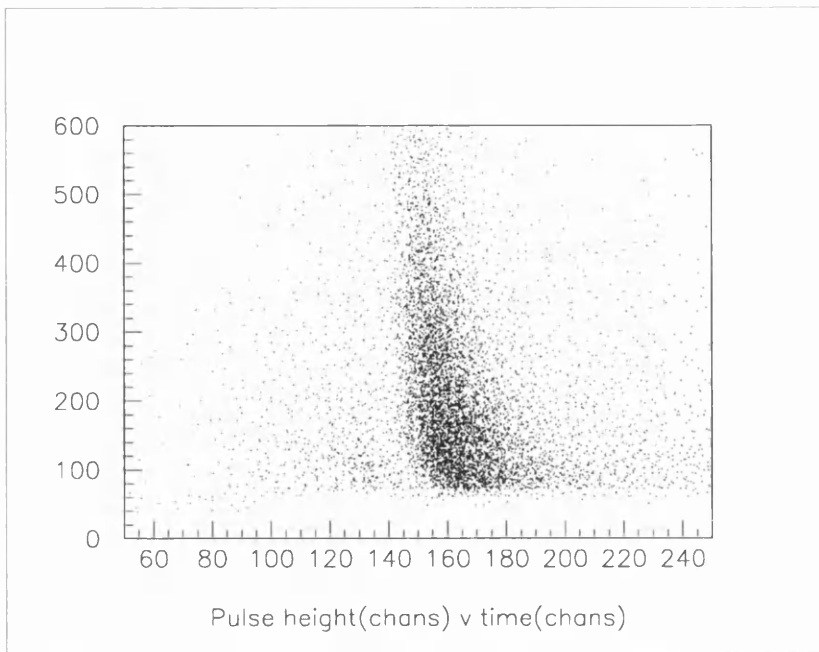


Figure 5.4: The walk effect in a neutron TDC.

The particles can interact at any point along the length of the block, thus smearing out the time signal at each end, and masking the walk effect. To remove this effect, a cut was applied around the spectrum formed from the difference of the TDC signals from the two ends of the block, so that the events were confined to a region of width approximately 10cm in the centre of the scintillator.

Applying such cuts to the data, we obtain Figure 5.5, showing  $\frac{1}{\sqrt{a}}$  plotted against time. The gradient of the relativistic ridge was measured by splitting the graph into regions of  $\frac{1}{\sqrt{a}}$  and noting the peak values of the TDC spectra for each of these regions. These peak values were plotted against  $\frac{1}{\sqrt{a}}$  and a least-squares fit applied to determine the gradient, from which the risetimes were calculated.

This procedure was repeated for all of the N1 blocks.

The N2 detectors are also subject to the effects of walk. Here data were already available for their risetimes. These detectors, which had been used previously in photo-nuclear experiments in the Mainz A2 collaboration, had their

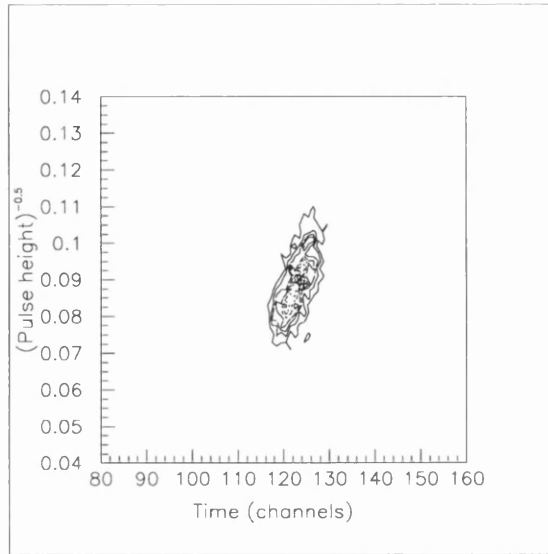


Figure 5.5:  $a^{-\frac{1}{2}}$  versus time

risetimes measured using a ‘flasher’ technique. The flashers emit pulses of light, normally of fixed amplitude, at regular intervals in order to provide a monitor of the detectors’ gain stability. They can also be used to measure risetimes by attenuating the pulses by varying degrees, and observing the resulting effect on the timing of the signals. This gives a more precise measurement of risetime than the method used here.

The risetimes of several N2 blocks were measured by the same method used for the N1 wall, and were found to be in good agreement with the values obtained by the ‘flasher’ method, thus also validating the procedure used for the N1 wall.

### 5.1.2 Position and time calibrations

The TDC information from the top and bottom of each block can now be combined by taking their mean value, providing a measurement of time-of-flight which is independent of the interaction position along the block. If we consider a block of length  $L$ , and a charged particle passing through the block at a distance  $x$

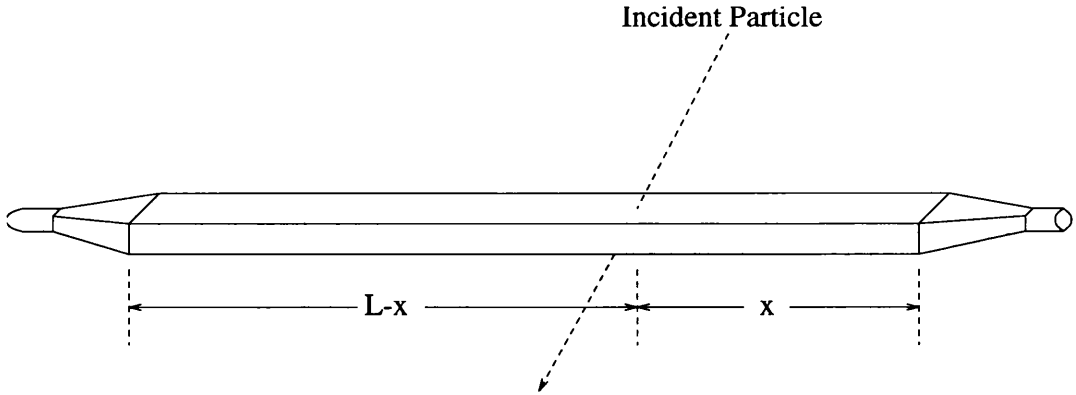


Figure 5.6: A scintillator block

from one end at a time  $t_0$ , then the time signals recorded at each end will be (see Figure 5.6.)

$$t_1 = t_0 + \frac{x}{v} \quad (5.3)$$

$$t_2 = t_0 + \frac{(L-x)}{v} \quad (5.4)$$

where  $v$  is the speed of propagation of a light pulse in the scintillator. Taking the mean of  $t_1$  and  $t_2$  we obtain

$$t_{mean} = t_0 + \frac{L}{2v} \quad (5.5)$$

which is independent of  $x$ . Similarly, considering the difference between the time signals we obtain a measurement of the position of the interaction.

$$t_{diff} = t_1 - t_2 = \frac{2x}{v} - \frac{L}{v} \quad (5.6)$$

A typical N1 mean time-of-flight spectrum, before and after the application of start and walk corrections, is shown in Figure 5.7. Note the appearance of the relativistic peak to the left of the neutron peak, which is not clearly visible in the uncorrected spectrum.

In order to calculate the kinetic energy of the neutrons, a knowledge of the time of the interaction with respect to the time origin of the event is required. The relativistic peak can be used to provide a channel in the TDC spectrum

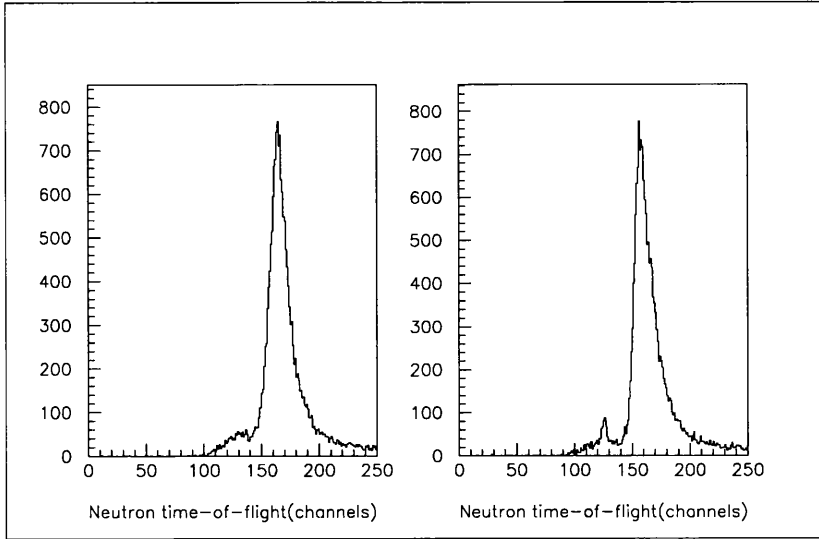


Figure 5.7: Neutron TDC spectra before and after time corrections.

which corresponds to a known point in time. The time taken for a relativistic particle to reach the detector is

$$t_{rel} = \frac{d}{c} \quad (5.7)$$

where  $d$  is the target-detector distance, and  $c$  is the velocity of light. Knowing the distance  $d$ , the time  $t_{rel}$  can be calculated, and equated with the channel at which the relativistic peak occurs.

The difference in channels between the relativistic peak and the neutron event can be converted to nanoseconds, and added to  $t_{rel}$ , giving, for each event, the time-of-flight of the neutron. Knowing the length of flight-path for each event, the neutron's velocity  $v$ , and hence kinetic energy  $T_n$ , can be calculated:

$$T_n = m_n (\gamma - 1) \quad (5.8)$$

where  $\gamma = (1 - \beta^2)^{-\frac{1}{2}}$  and  $\beta = \frac{v}{c}$ . Dedicated runs were made to detect such relativistic particles, which were also used in the pulse height calibration described in Section 5.7. An example of a TDC spectrum from such a run is shown in Figure 5.19.

A calibration of the TDC modules is required in order to convert TDC channels into time (nanoseconds). For this purpose, a time calibration unit was used. This unit generates two output pulses, one pulse acting as the start signal, and the second pulse occurring a time  $n\Delta$  later, where  $n$  is an integer and  $\Delta$  is a pre-determined time interval. Using the first signal to start the TDC modules and the second to provide the stop signal, a TDC spectrum of sharp spikes is obtained. Assuming the distance between adjacent spikes corresponds to  $\Delta$  ns, the gradient of a plot of time vs. channel will give the required conversion factor.

A position calibration is also required to convert the time difference in channels for each block into a distance in centimetres along the block. Here the solid angle of the magnet was used. The magnet has an aperture of  $\pm 5.7^\circ$  degrees subtended at the target, which will greatly reduce the number of neutrons at larger angles reaching the top and bottom of the scintillator blocks, resulting in a 'neutron shadow'. The length of region over which neutrons can be detected can be calculated for each detector, and compared with a time-difference spectrum from that block, giving us a calibration factor in channels/cm. This also lets us determine the channel in the time difference spectrum corresponding to a height  $y = 0$ . Any deviation from this channel can be converted into a height using the determined calibration factor. Figure 5.8 shows a typical time difference spectrum for an N1 detector.

The interaction position of each neutron is then known, and the neutron recoil angles  $\theta$  and  $\phi$  can be calculated (see Figure 5.9). Along with the kinetic energy of the neutron, this is all the information required from the N1 wall.

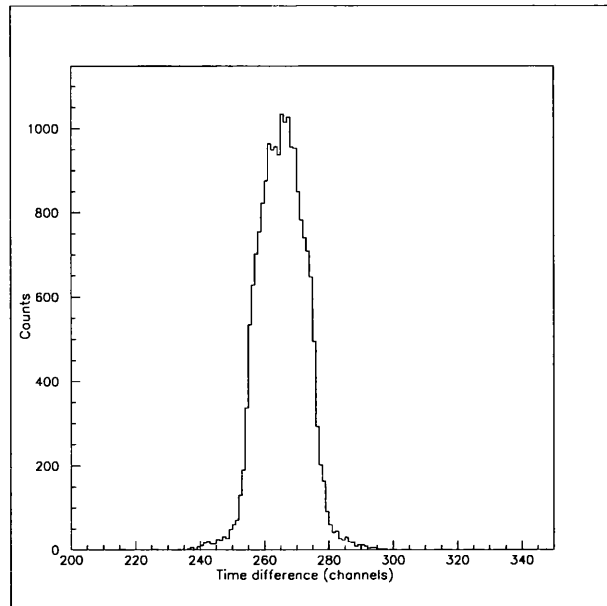


Figure 5.8: A neutron TDC spectrum

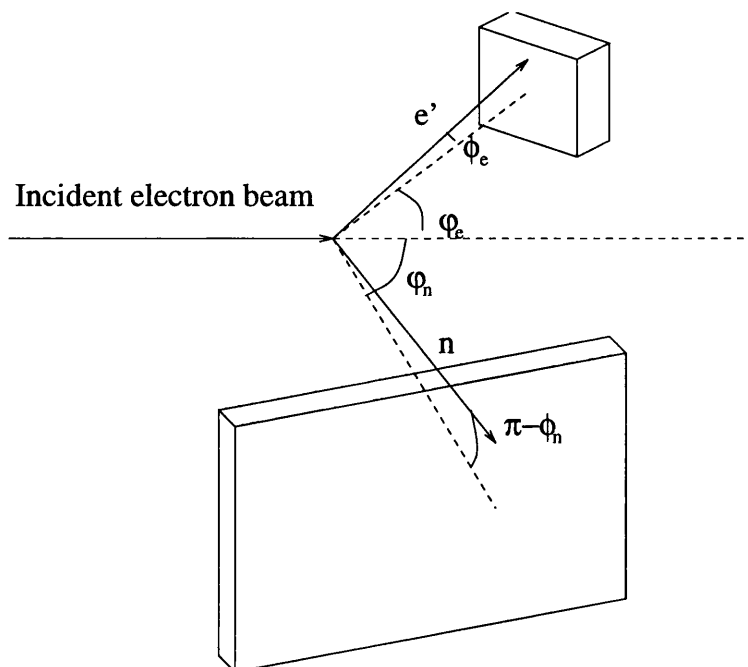


Figure 5.9: Scattering geometry

## 5.2 The electron detector

The lead-glass detector, described in section 3.6, provides us with position and energy information about the scattered electron. An electron will in general generate a light pulse in several neighbouring blocks in the array. Each block's coordinates with respect to the target are known, so knowing which block has been hit gives the electron's position, and hence its scattering angles (see Figure 5.9). The positional information can be improved over the 4 by 4cm dimensions of each block by utilising the pulse height information in the nearby blocks.

If  $q_i$  is the pulse height recorded in lead-glass block with coordinates  $x_i$  and  $y_i$ , and  $q_{sum}$  is the sum of the pulse heights recorded in the blocks, then defining  $Q_i = 3.5 + \log \frac{q_i}{q_{sum}}$  [52], the new weighted coordinates become

$$x = \frac{\sum_i Q_i x_i}{\sum_i Q_i} \quad (5.9)$$

and

$$y = \frac{\sum_i Q_i y_i}{\sum_i Q_i} \quad (5.10)$$

This gives a position resolution of  $\sim 0.7cm$ , corresponding to an angular resolution of  $< 0.3^\circ$ .

The electron scattering angle, combined with the neutron information and initial electron beam energy, allows us to determine fully the kinematics of the event, assuming that the  $D(e, e'n)$  reaction has occurred.

### 5.2.1 The lead-glass pulse height

A knowledge of the scattered electron energy is not necessary for a reconstruction of the kinematics, however the electron pulse height is useful in suppressing inelastic events ( $\pi$  production,  $\Delta$  resonances), which might otherwise have the same event 'signature'. These inelastic events will leave a much lower pulse in

the lead-glass array. To obtain the maximum information from this, the gains of the lead-glass blocks must be aligned in some way, as variations in the gains of the 256 lead-glass blocks will affect the 'lead-glass sum' spectrum and hence the contribution of inelastic events remaining after cuts on the lead-glass spectrum. Prior to the experiment taking place, the lead-glass gains were approximately aligned by considering the pulse-heights recorded in each of the 256 blocks. The full  $D(e, e'n)$  experiment took place over a period of several months, however, and so variations in gain with time must be considered. After selection of quasi-elastic events (section 5.3), the individual lead-glass spectra are observed and the position of the peak channel noted. A weighting factor can then be calculated which normalises the 256 peaks to the same channel.

As the electron detector covers an angle of  $\sim 18^\circ$ , the incident electron energy will vary across the face of the detector, hence smearing out the sum spectrum. As it is not necessary for the electron energy to be established from the lead-glass, but only to separate inelastic events from quasi-elastic events, an absolute energy calibration is unnecessary, and aligning the blocks by the above method improves the selection of quasi-elastic events.

An example of the lead-glass spectrum is shown in Figure 5.10, with the quasi-elastic and inelastic regions indicated. Due to the relatively poor energy resolution of the lead-glass ( $\sim 20\%$ ), it is not possible to distinguish clearly the quasi-elastic region. The spectrum is improved, however, by considering only the pulse heights in and around the block in which the maximum pulse height was recorded. This results in an improved spectrum, shown on the right of Figure 5.10.

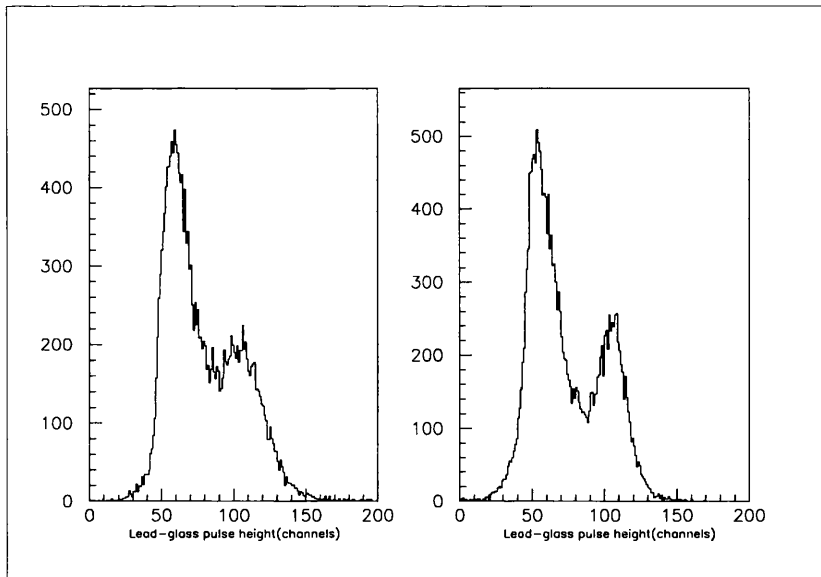


Figure 5.10: Left: The summed lead-glass pulse heights. Right: The sum of a cluster around the central block

### 5.3 Selection of quasi-elastic events

A cut on the lead-glass spectrum Figure 5.10 was applied to reject inelastic events, and cuts around the neutron time-of-flight spectra were made to select the neutron peaks. The measured neutron kinetic energy  $T_n$  can be compared to the kinetic energy calculated from the other kinematical information and assuming  $D(e, e'n)$  scattering has taken place,  $T_{th}$ . Figure 5.11 shows a histogram of the ratio  $R = \frac{T_n}{T_{th}}$ . Alongside this is a histogram of the same quantity obtained after application of cuts on the lead-glass sum at channel 90, and on the target proton momentum at 170 MeV/c. Figure 5.12 shows the same ratio obtained from the Monte-Carlo simulation of Chapter 4, i.e. for purely quasi-elastic scattering. Cuts on the experimentally measured ratio  $R$  were applied between 0.6 and 1.4.

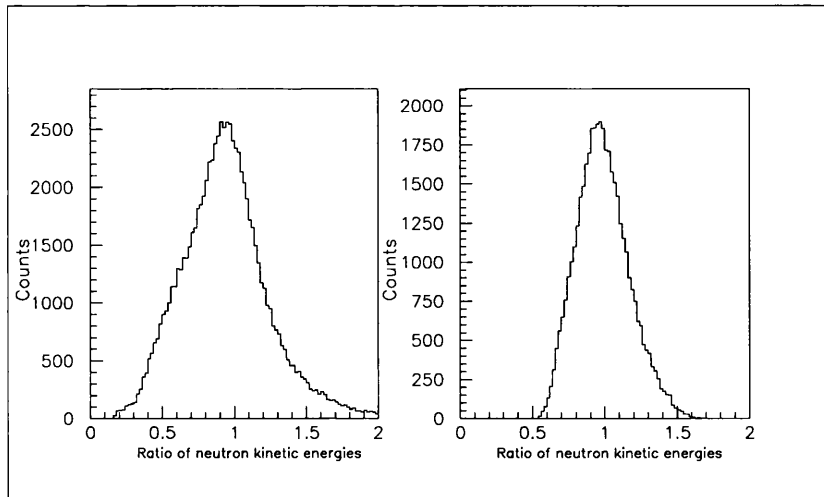


Figure 5.11: Ratio of measured neutron energy and that expected for free e-n scattering. Left: Without software cuts. Right: After application of cuts on electron pulse and proton momentum

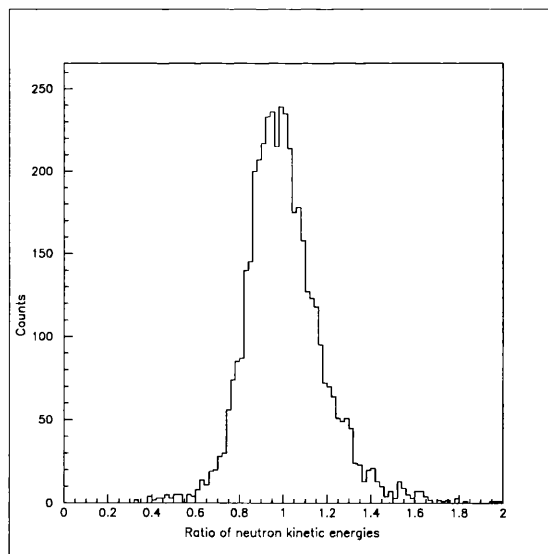


Figure 5.12: Ratio of measured neutron energy and that expected for free e-n scattering from Monte-Carlo simulation.

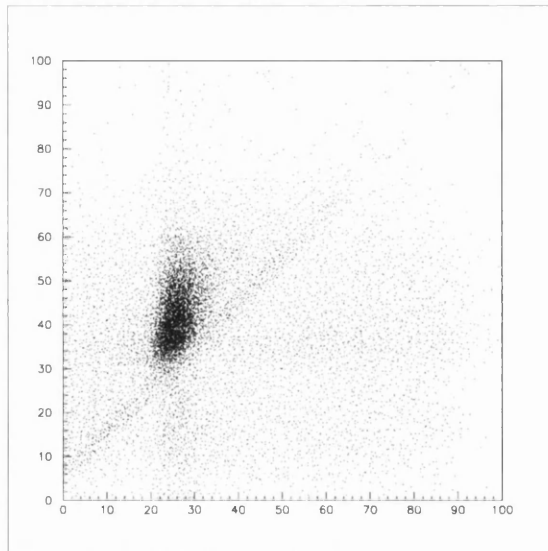


Figure 5.13: N2 time versus N1 time

## 5.4 Neutron Scattering Reconstruction

The neutron's angle of scattering between the N1 and N2 walls can now be reconstructed, and from that, an asymmetry deduced. Time-of-flight cuts can be applied to the N2 time spectra in a similar manner to those of the N1 wall. Before the application of these cuts, it is interesting to observe the distribution of events in the N1 time and N2 time domains (Figure 5.13). Here the area of interest to us, representing neutron double scattering, can be seen, with regions of accidental events in the N1 or N2 walls visible. For data taken under the application of a large magnetic field, these background regions are suppressed.

Those random background events under the N1-N2 coincidence peak will be included in the calculation of the asymmetry and will result in a lower asymmetry value, e.g. for the zero-field data, the random background contribution is estimated to be  $\sim 3\%$ , which will reduce the real asymmetry by the same fraction. The measured asymmetry must be corrected for this effect. No significant variation of background with  $\phi_n$  was observed.

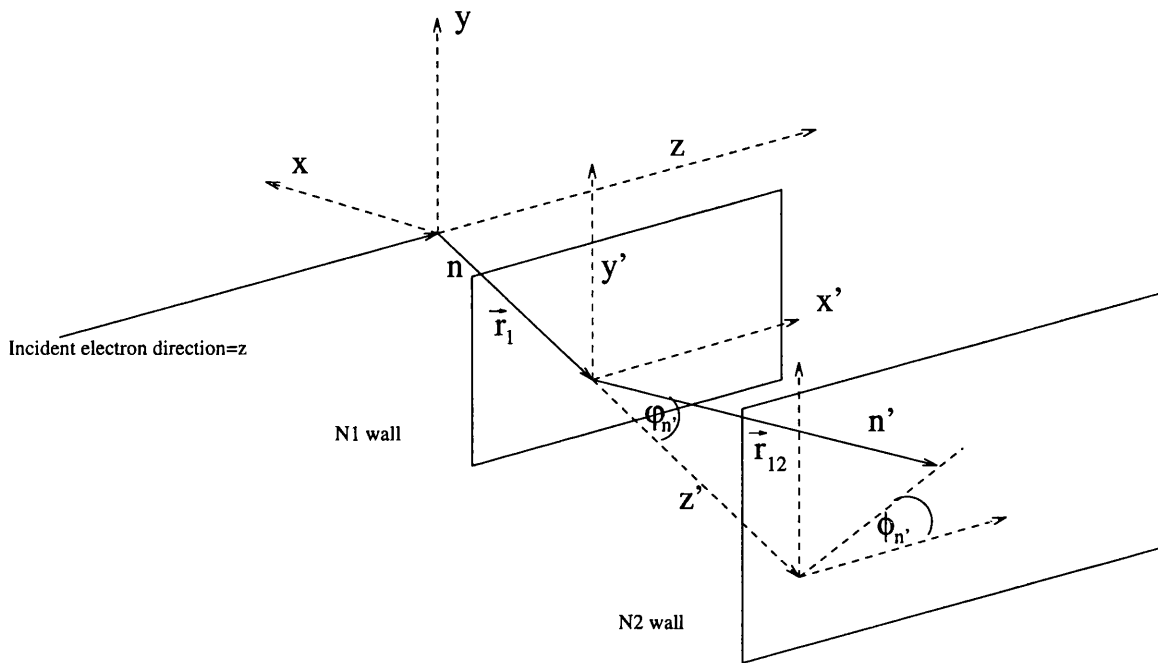


Figure 5.14: Double scattering geometry

Selecting the region of double neutron scattering, the scattered angles  $\theta_n'$  and  $\phi_n'$  can now be determined (Figure 5.14). Knowing the target-N1 and N1-N2 vectors  $\vec{r}_1$  and  $\vec{r}_{12}$  allows  $\theta_n'$  to be calculated. The choice of frame for  $\phi_n'$ , however, is not fixed, and depends on the initial neutron angles  $\theta_n$  and  $\phi_n$ . The initial neutron momentum vector can be described in terms of the unit vectors  $\vec{x}$ ,  $\vec{y}$  and  $\vec{z}$ ,  $\vec{z}$  being the initial electron direction vector. The angle  $\phi_n'$  is calculated in a new frame  $\vec{x}', \vec{y}', \vec{z}'$ , where  $\vec{z}'$  is in the direction of the initial neutron momentum vector  $\vec{p}_n$ ,  $\vec{y}'$  is formed from the vector product  $\vec{p}_n \times \vec{z}$ , and  $\vec{x}'$  is orthogonal to  $\vec{y}'$  and  $\vec{z}'$  and is equal to  $\vec{y}' \times \vec{z}'$ . The scattered angle  $\phi_n'$  is then calculated by projecting the vector  $\vec{p}_n'$  onto  $\vec{x}'$  and  $\vec{y}'$  such that  $\phi_n' = 0$  lies along the vector  $\vec{x}'$ , and  $\phi_n' = 90^\circ$  corresponds to the 'up' direction, i.e. along  $\vec{y}'$ .

The resulting  $\phi_n'$  distribution is shown in Figure 5.15. Note the loss of resolution at  $\phi_n' = 90^\circ$  and  $270^\circ$ , corresponding to the 'up' and 'down' directions,

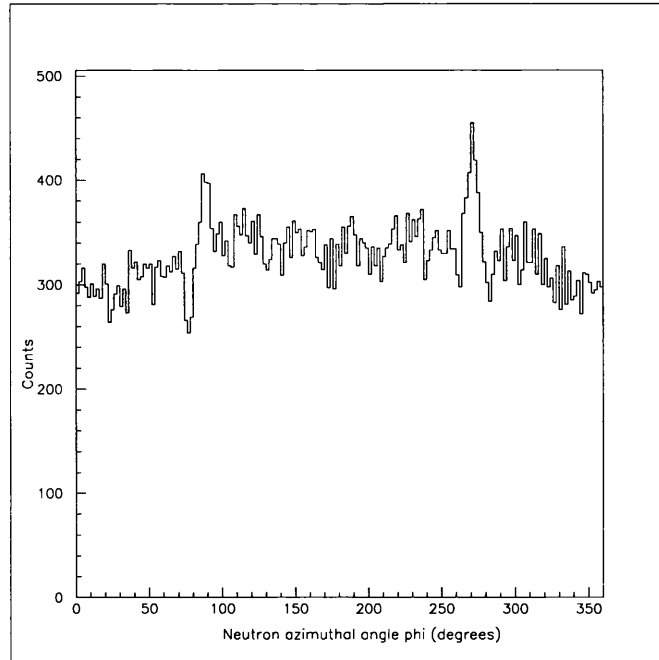


Figure 5.15: Neutron scattered angle  $\phi_n'$

where the segmented nature of the vertical blocks leads to the calculated angles becoming less continuous at these angles.

The above  $\phi_n'$  distribution is for all angles of  $\theta_n'$ , and as such encompasses a wide range of analysing powers. Referring to Figure 4.4, which shows the variation of analysing power,  $A$ , with  $\theta_n'$  and  $T_n$ , it will be seen that by restricting the angle  $\theta_n'$ , we can constrain ourselves to the region over which  $A$  is highest: following the results of the Monte-Carlo simulation, values of  $\theta_n'$  between  $10^\circ$  and  $40^\circ$  were selected (for all values of  $T_n$ ).

The resulting asymmetry as defined in Chapter 4 can now be calculated.

## 5.5 Asymmetry Calculation

The experimental procedure, as discussed in Chapter 4, is to measure an asymmetry over a wide range of spin-precession angles, giving us the ratio  $\frac{G_E}{G_M}$ , in-

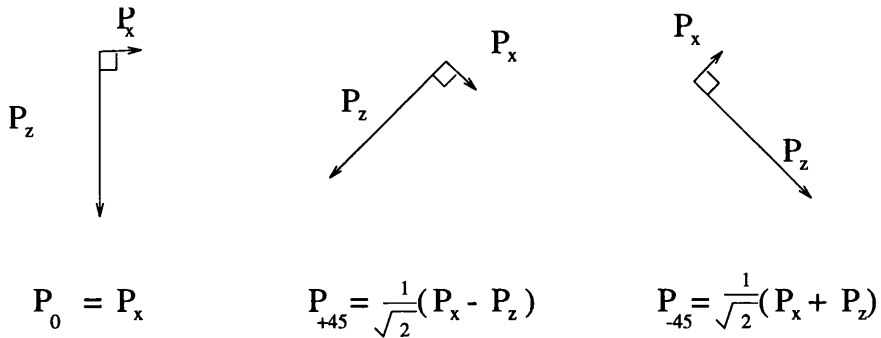


Figure 5.16: Polarisation vectors after  $45^\circ$  spin precession.

dependent of the analysing power  $A$ . As a preliminary test of the magnet and spin-precession method, data were taken during August 1995 with spin-precession angles of  $\pm 45^\circ$ . Under such conditions, the resultant transverse polarisation component  $P_X$  will take two different values, where the initial  $P_x^o$  and  $P_z^o$  components are rotated such that, when the resultant  $P_x$  component is formed, one obtains either a sum or a difference (see Figure 5.16). The possible resultant transverse polarisations are

$$P_{\pm 45} = P_x \cos 45^\circ \mp P_z \sin 45^\circ = \frac{P_x \mp P_z}{\sqrt{2}} \quad (5.11)$$

and the corresponding asymmetries will be

$$\mathcal{A}_{\pm 45} = \frac{A}{\sqrt{2}} (P_x \mp P_z) \quad (5.12)$$

where  $A$  is the analysing power. If we assume the dipole form for  $G_M$  giving a typical value of  $P_z \sim 0.5$ , and take a value for  $P_x$  of 0.07, then the expected asymmetries will be in the ratio  $\sim -0.75$ .

In this preliminary analysis, no timing or walk corrections were made, nor was any np/nC enrichment carried out, and so the resultant analysing power will be low. The resulting peak asymmetries, i.e. those formed from ‘up-down’ information only, (i.e. for angles of  $\phi_n'$  between 80 and 100 degrees and 170 and 190 degrees) were found to be  $(-2.2 \pm 0.9)\%$  and  $(+3.4 \pm 0.9)\%$ , in good agreement

with the expected ratio, and indicating an analysing power of approximately  $(8 \pm 2)\%$ . This is in good agreement with the expected analysing power from the Monte-Carlo simulation of Chapter 4 (see 4.3).

Following this test run, the full experiment was carried out, using spin-precessions of up to  $\pm 90^\circ$ .

## 5.6 Enrichment of n-p scattering events

In the analysis of the full data, the methods investigated in section 4.X were applied in order to improve the performance of the polarimeter. Before the application of such cuts, the asymmetries under  $-90^\circ$  spin-precession (i.e. that giving approximately the maximum transverse polarisation) are shown in Figure 5.17. The data are represented well by a sine curve. The curve shown is  $A \cos(\phi + \delta)$ ,  $\delta$  representing a phase shift and  $A$  the amplitude. ( $\delta = 0$  corresponding to  $A_y = 0$ ). The  $A_x$  component is found to be  $(3.03 \pm 0.23)\%$ , from which an analysing power of  $\sim 6\%$  can be deduced (assuming the dipole form for  $G_M$  at  $Q^2 = 9.4 \text{ fm}^{-2}$ , giving a polarisation  $P_z = 0.7$ , and a beam polarisation  $P_e = 0.7$ ).

The np/nC ratio can be improved by considering the information available to us in the polarimeter: the incident and scattered neutron energies  $T_n$  and  $T_{n'}$ , and the scattered neutron angle  $\theta_{n'}$ . In addition we require to know the proton recoil energy. This can be determined by considering the pulse height recorded by the QDC modules in the N1 wall. If it is assumed that the proton will come to rest in the N1 wall, then the pulse height recorded in the wall will be proportional to the proton energy. The Monte-Carlo simulation of Chapter 4 suggested that for the events of interest to us, over 90% of the protons will deposit all of their energy in the N1 wall. To convert the pulse height into a kinetic energy, a pulse height calibration is required.

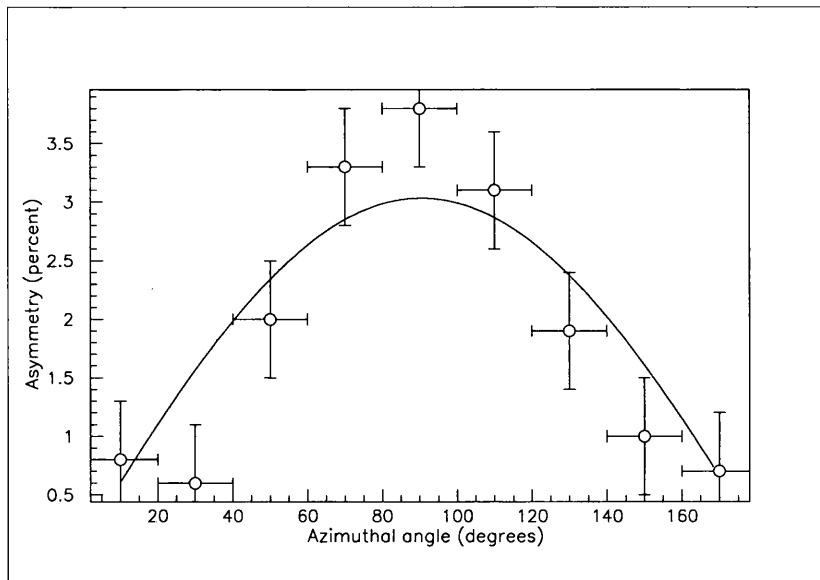


Figure 5.17: Asymmetry as a function of azimuthal angle.

## 5.7 Pulse-height Calibration

Two methods of pulse-height calibration are available to us. The first, by utilising cosmic rays passing through the polarimeter, and the second by using relativistic charged particles from the target. Both methods were employed here.

### 5.7.1 Cosmic Rays

The cosmic rays reaching the surface of the earth consist mainly of high-energy muons, providing a considerable flux of particles which, assuming they are minimum ionising, gives us a source of known energy deposition. The direction of these particles is mostly vertical, with the flux decreasing sharply at shallower angles. Sufficient particles are incident at shallow angles, however, to enable us to demand that a particle passes through all eight layers of the polarimeter. The flight path can then be reconstructed and hence the path length in each block calculated, allowing us to perform an energy calibration.

The trigger system was arranged to accept events where all eight layers of scintillator recorded a hit (while the electron beam was off). Using the methods described earlier, the positions of each hit were determined, and a software fitting routine was written and applied to the eight sets of coordinates in order to establish the angles of incidence and starting coordinate, from which the path length in each scintillator was calculated. By comparing the path length with the measured pulse height, the calibration factor can be obtained.

### 5.7.2 Droop corrections

The pulse height can be measured approximately independently of the position of interaction along the scintillator block by forming a geometric mean, (i.e. the square root of the product) of the pulse heights from the two ends. If the attenuation along a scintillator block can be described by an exponential decay curve, then we can write (see Figure 5.22)

$$q_1 = Aq_0e^{-\lambda x} \quad (5.13)$$

and

$$q_2 = Bq_0e^{-\lambda(L-x)} \quad (5.14)$$

where  $A$  and  $B$  are gain factors,  $q_0$  is the unattenuated pulse height,  $L$  is the length of scintillator block and  $x$  is the distance of the interaction from one end. Combining them in a geometric mean we obtain

$$q_{gm} = \sqrt{q_1q_2} = \sqrt{ABq_0^2e^{-\lambda L}} \quad (5.15)$$

which is proportional to the unattenuated pulse height  $q_0$ , and which is independent of  $x$ .

In practice the attenuation is not perfectly exponential, and so the geometric mean still exhibits a dependence on position, known as 'droop'. The top picture in

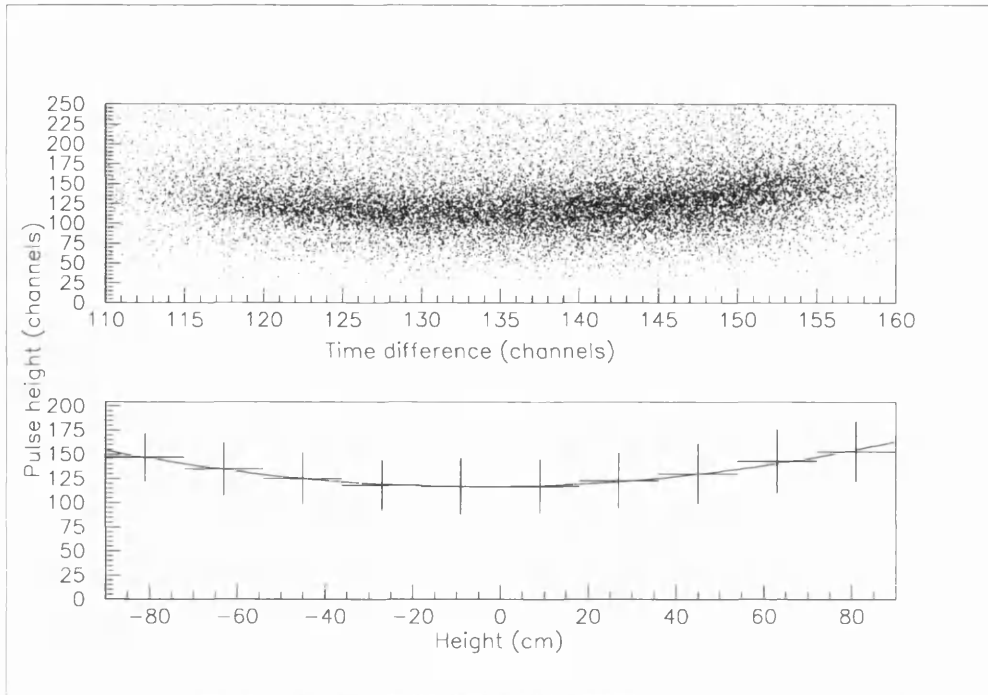


Figure 5.18: Parametrisation of droop in an N1 block.

Figure 5.18 shows the geometric mean pulse height, normalised to a path length of 10cm, plotted against the interaction position for one particular scintillator bar. The droop effect is clearly visible.

This effect can be corrected for by parametrising this droop curve. The data in the top picture of Figure 5.18 were split up into bins of width  $\sim 20\text{cm}$ , and for each bin the pulse height was observed and its peak channel noted. Plotting these peak channels against position  $x$ , we obtain the points shown in the lower part of Figure 5.18, to which a polynomial of the form  $a + bx + cx^2$  has been fitted. The parameters  $a, b$  and  $c$  were obtained for each block and the droop corrected for by normalising the pulse heights to the minimum point of each curve.

Following the droop correction, the pulse height calibration can be completed by observing the corrected pulse height, normalised to a path length of 10cm, and equating this with the energy deposited by a minimum ionising muon through

10cm of scintillator.

### 5.7.3 Relativistic particles

As the experiment was performed over a period of several months, fluctuations in the gains of the PM tubes may take place, affecting the energy calibration factors and hence the np/nC enrichment process. Calibration data in the form of relativistic particles from the target (during beam operation) were recorded, again by arranging the trigger to demand that particles passed through all layers of the polarimeter. This procedure was carried out as part of each experimental run, and the calibration data for the relevant runs were used in the subsequent analysis of the data.

The calibration figures are obtained in a similar way to the method described above for cosmic rays. A typical TDC spectrum from these calibration runs is shown in Figure 5.19. The relativistic peak can be seen to the left of the spectrum, around which cuts were applied to remove events not of interest to us. The resulting pulse height is corrected for droop using the parameters obtained above, and the vertical position of the interaction determined from TDC information. Assuming the particles originated at the target then the interaction position can tell us the angle, and hence the path-length in each block. Normalising the pulse heights to the same path length, the pulse height is equated with the energy deposited by a relativistic electron in 10cm of scintillator. The observed variations in gain with time were small, typically  $< 5\%$ .

### 5.7.4 The Enrichment Procedure

With the energy calibration complete, the enrichment procedures described in Chapter 4 can be carried out. The ratios  $Q_1$  and  $Q_2$  were formed (see equations

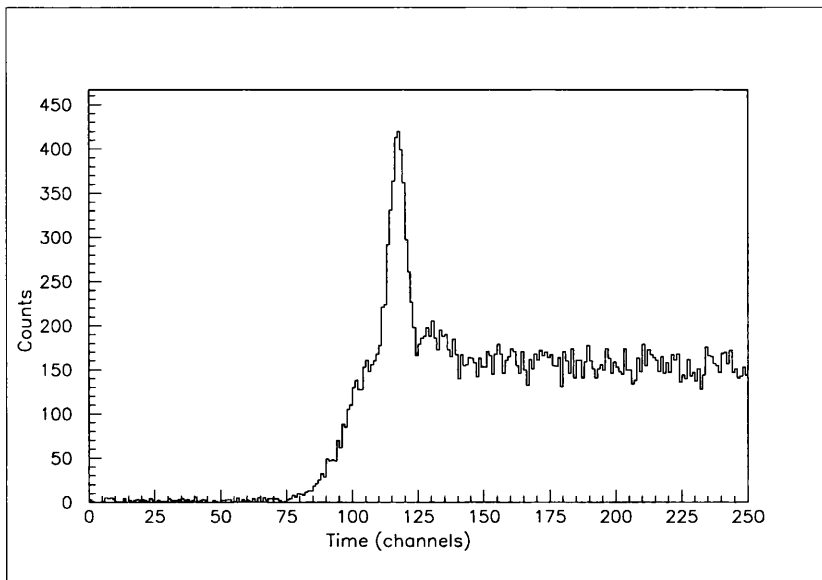


Figure 5.19: Relativistic peak in a neutron detector TDC spectrum.

4.15 and 4.16) and their influence on the observed asymmetries were investigated.

The quantities  $Q_1$  and  $Q_2$  are shown in Figure 5.20, and the same quantities obtained from the Monte-Carlo simulation are shown in Figure 5.21.

Applying cuts of  $0.1 < Q_1 < 1.4$  and  $0 < Q_2 < 1.8$  to the experimental data, (the regions which resulted in the most favourable Monte-Carlo results), the observed asymmetry increases to  $(5.4 \pm 0.4)\%$ , corresponding to an analysing power of  $(11.0 \pm 0.8)\%$ .

Asymmetries from  $90^\circ$  and  $0^\circ$  precession data, obtained by using various software cuts, and the analysing powers and  $\frac{G_E}{G_M}$  ratios obtained from them, are discussed in the following chapter.

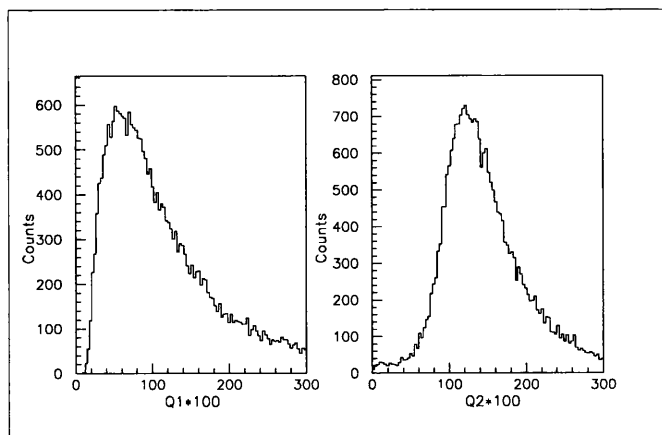


Figure 5.20: The ratios  $Q_1$  and  $Q_2$ .

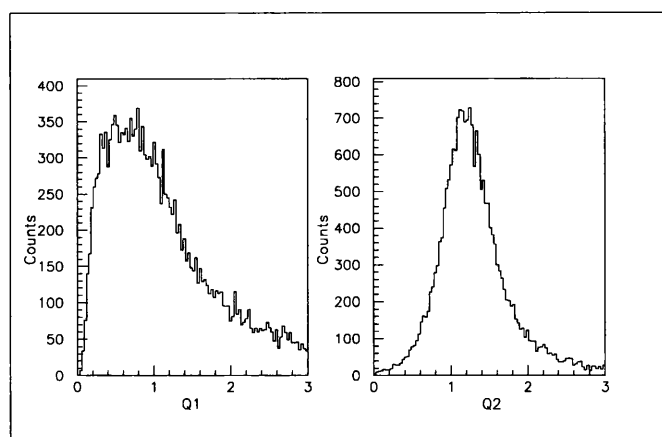


Figure 5.21: The ratios  $Q_1$  and  $Q_2$  from the MC simulation.

# Chapter 6

## Results and Conclusion

### 6.1 Polarimeter Analysing Power Measurement.

Using the data selection procedures described in Chapter 5, the asymmetries obtained under spin-precession of  $+90^\circ$  and  $-90^\circ$  were investigated. A typical asymmetry under spin-precession of  $-90^\circ$  is shown as a function of azimuthal scattering angle  $\phi$  in Figure 6.1. The asymmetry takes the form of a sine curve, which is expected for the case of  $A_y \sim 0$ . Fitting a function of the form  $A \sin(\phi + \delta)$  to the data, where  $A$  is the amplitude and  $\delta$  is a phase shift, allows us to extract the  $x$  and  $y$  components of the asymmetry:  $A_x = A \cos \delta$  and  $A_y = A \sin \delta$ .

The parameters obtained from Figure 6.1 are

$$A = (5.95 \pm 0.56)\% \text{ and } \delta = (2.6 \pm 5.0)^\circ.$$

From these we find

$$A_x = (5.94 \pm 0.56)\% \text{ and } A_y = (0.27 \pm 0.52)\%.$$

With the same conditions applied, the asymmetry under  $+90^\circ$  precession is

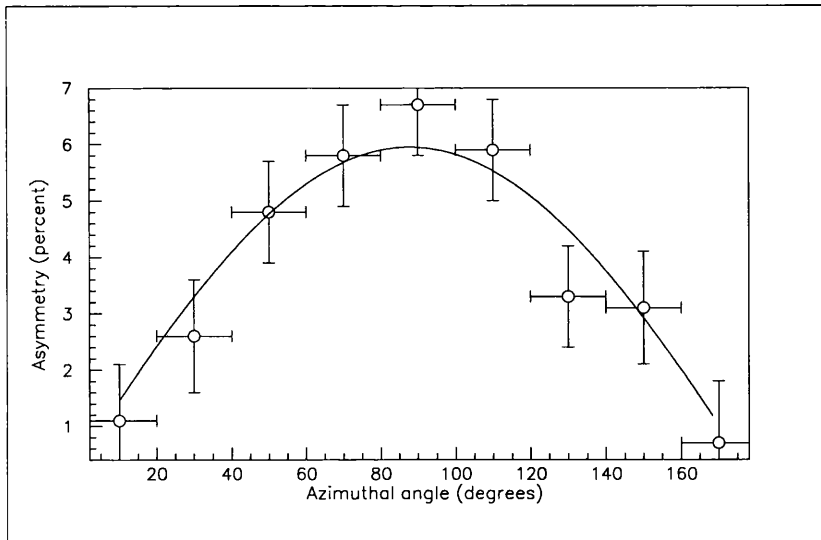


Figure 6.1: Asymmetry as a function of azimuthal angle.

shown in Figure 6.2. Here the values obtained are

$$A_x = (-7.33 \pm 0.69)\% \text{ and } A_y = (-0.27 \pm 0.68)\%$$

In general the  $A_y$  components are small and consistent with zero, as would be expected assuming the validity of equations 2.14-2.16 where  $P_y = 0$ . The  $A_x$  components would be expected to be equal and opposite, and, within the statistical errors of the above figures, this is the case. Assuming only a vertical field direction, any  $P_y$  component would be unaffected by the spin-precession and would give the same  $A_y$  value under positive and negative precessions. The smallness of the  $A_y$  components relative to their uncertainty makes it difficult to confirm this.

The possibility that the + and - field directions lead to different precession angles must be considered, e.g. a precession angle smaller than  $90^\circ$  would give rise to a smaller asymmetry. However in the region of  $90^\circ$  precession, a variation in precession angle of  $10^\circ$  would change the amplitude by 1.5%, much smaller

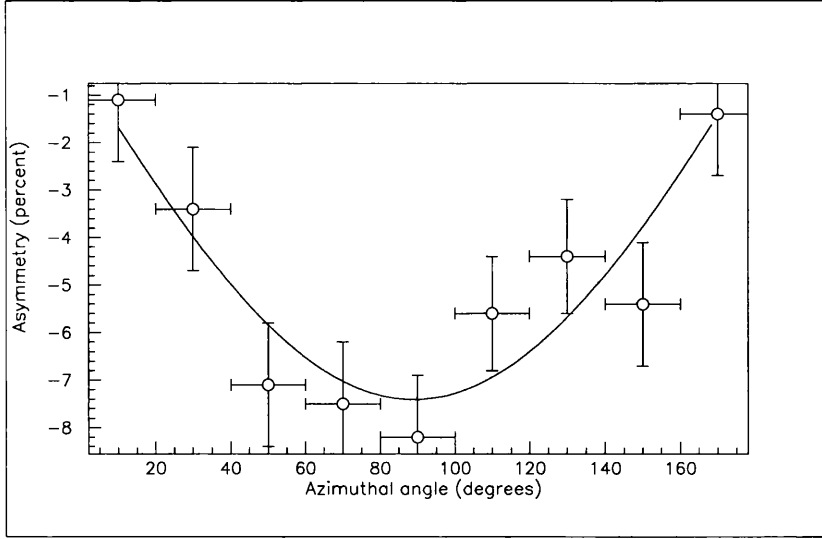


Figure 6.2: Asymmetry as a function of azimuthal angle.

than the statistical error in our measurements, ( $\frac{\Delta A_x}{A_x} \sim 9\%$ ).

Any variation in precession angle as a function of neutron trajectory can also be considered, e.g. the variation in neutron kinetic energy over the angular acceptance of the magnet will lead to a variation in transit time and hence to precession angle and amplitude. The effect of this for the range of neutron flight times of interest to us can be shown to be small, of the order of 1%, again smaller than the statistical errors here.

Taking a weighted average of the + and - asymmetries we obtain  $A_x = (6.49 \pm 0.43)\%$  which can be used to calculate the analysing power of the polarimeter. From equation 4.4, a component of polarisation  $P_x$  will result in an asymmetry  $A_x = \mathcal{A}P_x \sin \phi$ . Concerning ourselves only with the amplitude of the asymmetry, then we can say  $A_x = \mathcal{A}P_x$ . If we assume the neutron spin vector has undergone  $90^\circ$  precession then the measured polarisation  $P_x$  can be identified with the original  $P_z$  component defined as in equation 2.16, and which is calculable. Using the mean values of 4-momentum transfer squared and  $\theta_e$  in our measurement ( $\overline{Q^2} = 9.4 fm^{-2}$  and  $\overline{\theta_e} = 47.6^\circ$ , and assuming an electron

| Q1      | Q2      | $\mathcal{A}$  |
|---------|---------|----------------|
| 0.1-1.6 | 0.3-1.6 | $11.6 \pm 0.6$ |
| 0.1-1.4 | 0.3-1.6 | $12.3 \pm 0.7$ |
| 0.4-1.2 | 0.3-1.6 | $13.1 \pm 0.9$ |
| 0.2-1.2 | 0.3-1.6 | $13.3 \pm 0.6$ |
| 0.6-1.4 | 0.3-1.8 | $10.9 \pm 0.8$ |
| 0.7-1.2 | 0.3-1.8 | $11.4 \pm 0.9$ |
| 0.8-1.2 | 0.3-1.8 | $10.3 \pm 1.1$ |
| 0.2-1.2 | 0.3-1.2 | $17.4 \pm 0.9$ |

Table 6.1: Analysing power under various software cuts

polarisation of 70%), gives us  $P_z = 0.497$ .

The analysing power  $\mathcal{A}$  can now be calculated and is found to be

$$\mathcal{A} = (13.1 \pm 0.9)\%$$

The above value was obtained using n-p enrichment cuts on the variables  $Q_1$  and  $Q_2$  such that  $0.4 < Q_1 < 1.2$  and  $0.3 < Q_2 < 1.6$ . Values of analysing power obtained for various combinations of  $Q_1$  and  $Q_2$  are shown in Table 6.1 Here we have cut on the lead-glass sum spectrum (the right of Figure 5.10) at channel 90, and have selected values of  $\theta_{n'}$  between  $10^\circ$  and  $40^\circ$ .

The above results are in reasonable agreement with the predictions of the Monte-Carlo simulation of Chapter 4, given the statistical error of  $\sim 2 - 3\%$  on the simulation results. Here the maximum Analysing Powers obtained were around 16 – 18%, with the optimum Figure of Merits found with slightly lower Analysing Powers of around 14%.

This suggests that there is little contribution to the Analysing Power from n-C interactions in the scintillator.

| Q1      | Q2      | $G_E^n$           |
|---------|---------|-------------------|
| 0.1-1.6 | 0.3-1.6 | $0.055 \pm 0.010$ |
| 0.4-1.2 | 0.3-1.6 | $0.052 \pm 0.011$ |
| 0.4-1.2 | 0.3-2.0 | $0.045 \pm 0.011$ |
| 0.1-1.6 | 0.3-2.0 | $0.048 \pm 0.011$ |

Table 6.2:  $G_E^n$  under various software cuts

## 6.2 Zero-Field Asymmetries and $G_E^n$

Data taken with no spin-precessing magnetic field applied were analysed in a similar manner. The best statistical precision on  $A_x$  was found with the conditions  $0.1 < Q_1 < 1.6$  and  $0.3 < Q_2 < 1.6$ , giving

$$A_x = (1.11 \pm 0.20)\% \text{ with } \chi^2 = 1.07.$$

Varying the enrichment cuts around these values did not greatly alter the precision of  $A_x$  ( $\frac{\Delta A_x}{A_x} \sim 0.20$ ).

The 90 and 0-degree asymmetries can now be combined to form the ratio  $\frac{G_E}{G_M}$ . Referring to equation 4.7 we can say that

$$\frac{A_x^0}{A_x^{90}} = \kappa \frac{G_E}{G_M}$$

where  $\kappa$  is a kinematical factor. Using the mean values calculated for the kinematical factor, and the dipole form for  $G_M$ , then  $G_E$  can be calculated. Values of  $G_E$  found under various enrichment cuts are given in Table 6.2

These are consistent within the accuracy of the measurements, as is expected, as these cuts should vary only the analysing power, which cancels out of the  $G_E$  calculation. These figures were obtained after cutting the lead-glass spectrum (Figure 5.10) on channel 90. The effect of varying this cut has been investigated: (Table 6.3)

| Lead-glass pulse | $\mathcal{A}$ | $G_E^n$           |
|------------------|---------------|-------------------|
| >75              | 10.1          | $0.058 \pm 0.011$ |
| >80              | 10.4          | $0.059 \pm 0.011$ |
| >90              | 11.6          | $0.055 \pm 0.010$ |
| >100             | 13.4          | $0.048 \pm 0.011$ |
| >110             | 13.0          | $0.044 \pm 0.016$ |
| 75-95            | 5.1           | $0.102 \pm 0.044$ |
| 95-110           | 10.8          | $0.061 \pm 0.016$ |
| >110             | 13.0          | $0.044 \pm 0.016$ |

Table 6.3: The effect of electron pulse height cuts on  $G_E^n$ 

Here we encounter larger variations in  $G_E$ , although the statistical precision is much poorer in some cases. Making such cuts on the lead-glass might be expected to vary the proportion of inelastic events included in the data. Varying the cut between channels 80 and 100 does not significantly affect the values obtained, however.

### 6.3 Nuclear Binding Effects

The relationships used to extract  $P_x$  and hence  $G_E$  are strictly true only for free-neutron scattering. In the case of a neutron bound in Deuterium, nuclear binding effects may alter the relationship and invalidate equations 2.14-2.16 to some extent. As discussed in Chapter 2, such effects will be small in the region where  $\theta_{nq}$  is small. The angles  $\theta_{nq}$  and  $\phi_r$  are defined in Figure 6.3 and the measured distributions are shown in Figure 6.4.

The dependence of polarisation transfer on  $\theta_{nq}$  (the angle between the neutron momentum vector  $p_n$  and the momentum transfer vector  $q$ ) and  $\phi_r$  (the azimuthal

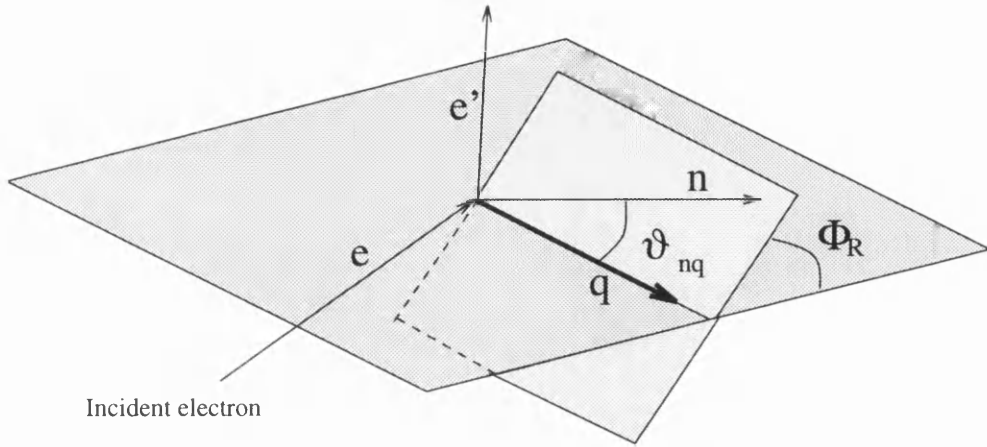


Figure 6.3: The angles  $\theta_{nq}$  and  $\phi_r$ .

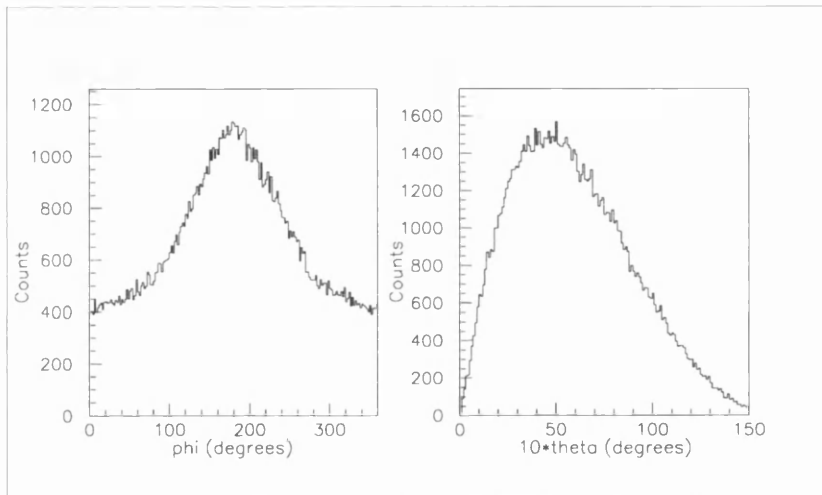


Figure 6.4: The  $\phi_r$  (left) and  $\theta_{nq}$  (right) distributions.

angle between  $p_n$  and  $q$  were investigated theoretically by Arenhövel [22]

The experimental dependence of  $P_x$  (which is proportional to our  $G_E$  value) on  $\theta_{nq}$  and  $\phi_r$  can be investigated here. The effect of  $\theta_{nq}$  cuts on  $G_E$  is shown in Table 6.4 The values of  $G_E$  vary considerably over the range 0 to  $9^\circ$ , although the large statistical error on these values make it difficult to draw any firm conclusions. Applying increasing upper limits on  $\theta_{nq}$  has only a small effect on the average  $G_E$  value, due to the small number of events at large values of  $\theta_{nq}$ .

| $\theta_{nq}$ | $\mathcal{A}$ | $G_E^n$           |
|---------------|---------------|-------------------|
| 0-3           | 10.9          | $0.080 \pm 0.026$ |
| 3-6           | 11.0          | $0.038 \pm 0.018$ |
| 6-9           | 11.5          | $0.068 \pm 0.023$ |
| >9            | 15.6          | $0.029 \pm 0.019$ |
| 0-6           | 10.8          | $0.052 \pm 0.015$ |
| 0-9           | 10.9          | $0.057 \pm 0.013$ |
| 0-20          | 11.6          | $0.055 \pm 0.010$ |

Table 6.4:  $\theta_{nq}$  dependence of  $G_E^n$ 

The dependence of the measured  $G_E$  value on  $\phi_r$  is shown in Table 6.5. Again due to statistics, it is difficult to draw any conclusions about any  $\phi_r$  dependence. The variation of  $P_x$  with  $\theta_{nq}$  was investigated by Arenhövel and are shown in [21] for values of  $\phi_r \sim 0^\circ$  and  $\phi_r \sim 180^\circ$ . This predicts a falling  $P_x$  with increasing  $\theta_{nq}$  for  $\phi \sim 0^\circ$  and a rising  $P_x$  with increasing  $\theta_{nq}$  for  $\phi \sim 180^\circ$ . From the figures below (Table 6.6) there is some evidence to support this.

## 6.4 Sources of systematic error

The lead wall, situated on the target side of the magnet, is designed to stop any protons from the target from reaching the polarimeter. It is possible for some of these protons to undergo charge-exchange in the lead-wall and emerge as neutrons which might be identified in the polarimeter as quasi-elastic D(e,e'n)p events. The possible size of this contribution was investigated in an earlier A3 pilot experiment [53]. The size of the contribution was estimated to be  $\leq 3\%$ . The protons will possess a larger  $P_x$  component ( $\sim 30\%$ ); assuming transfer of all this polarisation to the neutron would result in a contribution of  $\leq 10\%$  to

| $\phi_r$ | $G_E^n$           |
|----------|-------------------|
| 0-44     | $0.056 \pm 0.045$ |
| 45-89    | $0.069 \pm 0.058$ |
| 90-134   | $0.024 \pm 0.024$ |
| 135-179  | $0.070 \pm 0.021$ |
| 180-224  | $0.043 \pm 0.022$ |
| 225-269  | $0.056 \pm 0.026$ |
| 270-314  | $0.071 \pm 0.033$ |
| 315-359  | $0.061 \pm 0.024$ |

Table 6.5:  $\phi_r$  dependence of  $G_E^n$ 

| $\phi_r$ | all $\theta_{nq}$ | $\theta_{nq} < 3$ | $\theta_{nq} 3 - 6$ | $\theta_{nq} > 3$ |
|----------|-------------------|-------------------|---------------------|-------------------|
| 315-44   | $0.069 \pm 0.029$ | $0.121 \pm 0.062$ | $0.033 \pm 0.029$   | $0.014 \pm 0.025$ |
| 135-224  | $0.055 \pm 0.016$ | $0.122 \pm 0.045$ | $0.038 \pm 0.027$   | $0.050 \pm 0.016$ |

Table 6.6:  $\phi_r$  and  $\theta_{nq}$  dependence of  $G_E^n$

the measured neutron polarisation. For the case of zero-field precession, this will have a small effect on the uncertainty in  $P_x$  where the statistical uncertainty is  $\sim 20\%$ . For the  $90^\circ$  precession case, however, this could have a larger effect on our measured  $P_x$  where the statistical error is  $\sim 6\%$ , although this effect will be lessened by the larger value of  $P_z$ . It is possible that any stray magnetic field may deflect some of the protons before reaching the lead wall, although the effect of this on the precession and hence the polarisation component of any resulting neutrons is more difficult to estimate.

As discussed in Chapter 4, the calculated asymmetry is independent of beam luminosity and of detector efficiency, and by using the spin-precession method, both the absolute value of beam polarisation and the analysing power of the polarimeter cancel out. Variations in beam polarisation between the  $90^\circ$  and zero-field data sets must be considered however and can be estimated to be  $\sim 5\%$ . Variation of N1 gain is important in the n-p enrichment process, however measured variation in the N1 gains were small, and the dominant uncertainty in the  $Q$  ratios originated in the time-of-flight measurements. Varying the  $Q$  cuts used resulted in variations to  $G_E^n$  of around 10%. The lead-glass gain was found to have significant variations of gain with time ( $\sim 10\%$ ) but the effect of varying the lead-glass threshold on the measured  $P_x$  component was found to be small  $\sim 5\%$ . The spin-precession angle depends on the magnetic field stability; however, as discussed earlier, any variation of precession angle around the  $90^\circ$  point will have only a small relative variation in the polarisation components. This may have a larger effect on the intermediate precession angles used in the analysis of the full data-set. Variations of the field integral for various neutron trajectories was estimated by measuring the field at several points on different trajectories. The observed variation was small ( $< 3\%$ ). Considering all these contributions, an overall systematic uncertainty can be estimated to be  $\sim 18\%$ . This gives us a

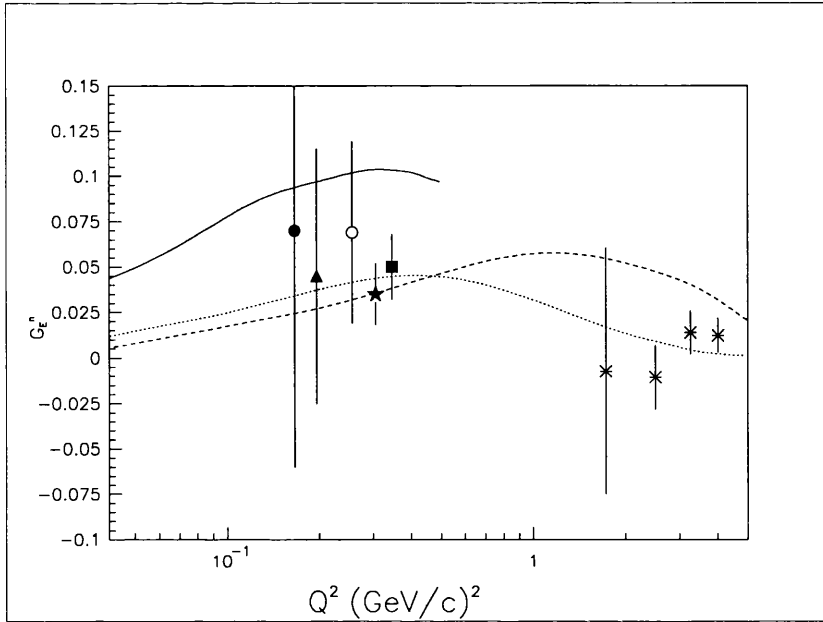


Figure 6.5:  $G_E^n$  : The result of the present measurement is indicated by the filled square. The other data points are as follows: Jones-Woodward [35] (filled circle), Thompson [34] (triangle), Eden [33] (open circle), Meyerhoff [20] (star) and Lung [15] (asterisks). Theoretical curves of Gorski [31] (solid), Cardarelli [32] (dotted) and Gari and Krümpelmann [27] (dashed) are also shown.

value of  $G_E^n$  of  $0.050 \pm 0.011 \pm 0.009$  at  $Q^2 = 9.4 fm^{-2}$ . This value is shown in Figure 6.5, along with the recent measurements and theoretical calculations of Figure 2.3. The value obtained here is consistent with that of the pilot  ${}^3He$  Mainz experiment (at a slightly lower  $Q^2$ ) and offers greater statistical precision than other recent polarisation measurements. Moreover the result is not subject to the same large systematic uncertainty associated with the measurements of [9]. The result is consistent with the theoretical curves of both [27] and [32], but is unable to distinguish between the two. Improved measurements at higher  $Q^2$  would be required to do this. The curve of [31] would appear to be discounted by this result.

## 6.5 Conclusion

A Monte-Carlo simulation of a neutron polarimeter was carried out which helped to establish the optimum methods of data analysis of the real experiment. The simulation findings were in good agreement with those of a previous independent simulation, and in good agreement with the results of the analysing power measurement using the spin-precession method. The time resolution obtained,  $\sim 2ns$ , was not sufficient to achieve the analysing powers of  $\geq 20\%$  which could be achieved with a better time resolution. The simulation assumed no contribution from Carbon to the analysing power, and the agreement with the experimental measurement (which is independent of our knowledge of  $G_E^n$ ) implies that the Carbon does indeed contribute little to the overall analysing power of the polarimeter.

A preliminary value of  $G_E^n$  was obtained which is in good agreement with recent model-independent measurements using polarised beams, although the statistical uncertainty here and in earlier measurements is large. Little dependence on  $\theta_{nq}$  or  $\phi_R$  was found, although the statistics for these investigations were limited. The value of  $G_E^n = 0.050 \pm 0.011 \pm 0.009$  was obtained at an average value of  $Q^2 = 9.4 fm^{-2}$ .

Analysis of the full data set, (i.e. using a range of intermediate precession angles in addition to  $90^\circ$  and  $0^\circ$ ), will provide a more precise measurement of  $G_E^n$  and will enable a more thorough investigation of the effects of nuclear binding on the polarisation observables. This, in combination with the result from the related  ${}^3He$  experiment, and from similar experiments taking place at other laboratories, will provide useful new information on the structure of the neutron.

# Bibliography

- [1] Particle Data Group, American Institute of Physics, (1994)
- [2] R.Gähler *et al.*, Physical Review D25 (1982) 2887
- [3] J.M.Robson, Physical Review 83 (1951) 349
- [4] L.W.Alvarez and F.Bloch, Physical Review 57 (1940) 111
- [5] G.L.Green *et al.*, Physical Review D20 (1979) 2139
- [6] M.N.Rosenbluth, Physical Review 79 (1950) 615
- [7] H.Leeb and C.Teichtmeister, Physical Review C48 (1993) 1719
- [8] S.Kopecky *et al.*, Physical Review Letters 74 (1995) 2427
- [9] S.Platchkov *et al.*, Nuclear Physics A510 (1990) 740
- [10] S.Galster *et al.*, Nuclear Physics B32 (1971) 221
- [11] M.Lacombe *et al.* Physics Letters B101 (1981) 139
- [12] R.V.Reid, Ann. of Phys. 50 (1968) 411
- [13] R.Budnitz *et al.*, Physical Review Letters 19 (1967) 809
- [14] W.Bartel *et al.*, Nuclear Physics B58 (1973) 429
- [15] A.Lung *et al.*, Physical Review Letters 70 (1993) 718

- [16] E.E.W.Bruins *et al.*, Physical Review Letters 75 (1995) 21
- [17] H.Anklin *et al.*, Physics Letters B336 (1994) 313
- [18] T.W.Donnelly and A.S.Raskin, Annals of Physics 169 (1986) 247
- [19] R.G.Arnold *et al.*, Physical Review C23 (1981) 363
- [20] M.Meyerhoff *et al.*, Physics Letters B327 (1994) 201
- [21] A. Frey, Doctoral Thesis, Johannes Gutenberg Universitat Mainz, (1994)
- [22] H.Arenhövel, Physics Letters B199 (1987) 13
- [23] J.Laget, Physics Letters B273 (1991) 367
- [24] D.Eyl *et al.*, Zeitschrift für Physik A352 (1995) 211
- [25] G.Höhler *et al.*, Nuclear Physics B114 (1976) 505
- [26] M.Gari and W.Krümpelmann, Zeitschrift für Physik A322 (1985) 689
- [27] M.Gari and W.Krümpelmann, Physics Letters B173 (1986) 173
- [28] P.L.Chung and F.Coester, Physical Review D44 (1991) 229
- [29] A.V.Radyushkin, Acta.Phys.Pol B15 (1984) 304
- [30] G.W.Botz, P.Haberl and O.Nachtmann, Zeit.Phys. C67 (1995) 143
- [31] A.Z.Gorski *et al.*, Physics Letters B 278 (1992) 24
- [32] F.Cardarelli *et al.*, Physics Letters B 357 (1995) 267
- [33] T.Eden *et al.*, Physical Review C 50 (1994) R1749
- [34] A.K.Thompson *et al.*, Physical Review Letters 68 (1992) 2901

- [35] C.E.Jones-Woodward *et al.*, Physical Review C44 (1991) R571
- [36] H.Herminghaus *et al.*, *Proc. Linear Accelerator Conference*, Albuquerque, (1990).
- [37] K.H.Steffens *et al.*, NIM A325 (1993) 378
- [38] B.Wagner *et al.*, NIM A294 (1990) 541
- [39] FASTBUS Modular High Speed Data Acquisition and Control System, ANSI/IEEE std 960-1986.
- [40] CAMAC A Modular Instrumentation System for Data Handling, EUR 4100e (1972)
- [41] The VME-bus specification, ANSI/IEEE std 1014-1987.
- [42] J.R.M.Annand *et al.*, NIM A262 (1987) 329
- [43] R.A.Arndt *et al.*, Physical Review C15 (1977) 1002
- [44] V.Bargmann *et al.*, Phys.Rev.Letters 2 (1959) 435
- [45] GEANT 3.21 Simulation Package, CERN, Geneva (1994)
- [46] R.A.Cecil *et al.*, NIM 161 (1979) 439
- [47] S.Cierjacks *et al.*, NIM 192 (1982) 407
- [48] M.Bernheim *et al.*, Nuclear Physics A365 (1981) 349
- [49] G.G.Ohlsen and P.W.Keaton Jr., Nucl.Instrum.Methods 109 (1973) 41
- [50] J.R.M.Annand, *Kelvin Lab Internal Report*
- [51] W.Braunschweig *et al.* NIM 134 (1976) 261

[52] D.Eyl, Doctoral Thesis, Johannes Gutenberg Universität Mainz, (1993).

[53] M.Ostrick, Diplomarbeit, Johannes Gutenberg Universität Mainz, (1994)

